The representation of sea salt aerosols and their role in polar climate within CMIP6

Rémy Lapere[1], Jennie L. Thomas[1], Louis Marelle[2], Annica M. L. Ekman[3,4], Markus M. Frey[5], Marianne Tronstad Lund[6], Risto Makkonen[7], Ananth Ranjithkumar[5], Matthew E. Salter[3,8], Bjørn Hallvard Samset[6], Michael Schulz[9], Larisa Sogacheva[7], Xin Yang[5], Paul Zieger[3,8]

[1]Univ. Grenoble Alpes, CNRS, IRD, Grenoble INP*, IGE, 38000 Grenoble, France
[2]LATMOS/IPSL, Sorbonne Université, UVSQ, CNRS, Paris, France
[3]Department of Meteorology, Stockholm University, Stockholm, Sweden
[4]Bolin Center for Climate Research, Stockholm, Sweden
[5]Natural Environment Research Council, British Antarctic Survey, Cambridge, UK
[6]CICERO Center for International Climate Research, Oslo, Norway
[7]Finnish Meteorological Institute, Climate Research Programme, Helsinki, Finland
[8]Department of Environmental Science, Stockholm University, Stockholm, Sweden
[9]Norwegian Meteorological Institute, Oslo, Norway
*Institute of Engineering and Management Univ. Grenoble Alpes

Key Points:

- CMIP6 models have a large uncertainty in present day sea salt aerosol abundance at the poles
- Model performance is degraded closer to the poles suggesting inadequate emissions sources within the polar regions
- Both present and future radiative balance at the poles is uncertain because of sea salt aerosols

Corresponding author: Rémy Lapere, remy.lapere@univ-grenoble-alpes.fr

Corresponding author: Jennie L. Thomas, jennie.thomas@univ-grenoble-alpes.fr

Abstract

Natural aerosols and their interactions with clouds remain an important uncertainty within climate models, especially at the poles. Here, we study the behavior of sea salt aerosols (SSaer) in the Arctic and Antarctic within 12 climate models from CMIP6. We investigate the driving factors that control SSaer abundances and show large differences based on the choice of the source function, and the representation of aerosol processes in the atmosphere. Close to the poles, the CMIP6 models do not match observed seasonal cycles of surface concentrations, likely due to the absence of wintertime SSaer sources such as blowing snow. Further away from the poles, simulated concentrations have the correct seasonality, but have a positive mean bias of up to one order of magnitude. SSaer optical depth is derived from the MODIS data and compared to modeled values, revealing good agreement, except for winter months. Better agreement for AOD than surface concentration may indicate a need for improving the vertical distribution, the size distribution and/or hygroscopicity of modeled polar SSaer. Source functions used in CMIP6 emit very different numbers of small SSaer, potentially exacerbating cloud-aerosol interaction uncertainties in these remote regions. For future climate scenarios SSP126 and SSP585, we show that SSaer concentrations increase at both poles at the end of the 21^{st} century, with more than two times mid-20^{th} century values in the Arctic. The pre-industrial climate CMIP6 experiments suggest there is a large uncertainty in the polar radiative budget due to SSaer.

1 Introduction

The polar regions have a larger sensitivity to changes in global climate than any other region (Manabe & Wetherald, 1975; Meredith et al., 2019). This is called polar amplification, which refers to the multiple factors that control why polar regions are changing faster than the rest of the planet. A key reason for polar amplification is sea ice and snow loss, which changes surface albedo from light to dark and induces an additional regional warming, or climate feedback (Hall, 2004). Atmospheric temperature feedbacks such as the Planck feedback and local lapse-rate feedback also play an important role in this amplification (Stuecker et al., 2018). Rantanen et al. (2022) found that climate models and observational data disagree on the magnitude of Arctic amplification over the past 40 years, with larger trends found in observations. Climate models capture some aspects of polar amplification, but not all of the complexity of what is occurring within the rapidly changing polar regions, in particular in the Antarctic where the model bias is even more pronounced (D. M. Smith et al., 2019).

Clouds are a key, uncertain component of the polar and global climate system (Flato et al., 2013). Specifically, clouds can have both a cooling (via reflection of shortwave radiation) and warming (by trapping longwave radiation) effect on the polar atmosphere, depending on their optical thickness and cloud droplet number as reviewed in Alkama et al. (2020). As a result, polar clouds in summer have the potential to dampen the radiative impact of sea ice loss through shortwave cooling (Alkama et al., 2020), but summertime low-level clouds in the Arctic can also favor sea ice melt through longwave warming (Y. Huang et al., 2021). In wintertime, the surface cloud forcing at the poles is stronger than in summer and with a warming effect (Curry et al., 1996).

Aerosols are also a key uncertainty in climate models globally and have even larger uncertainties in the polar regions (Sand et al., 2017). Aerosols influence the climate through their interaction with radiation directly (aerosol direct effect) and their role in cloud formation/modification (aerosol indirect and semi-direct effects) (Myhre et al., 2013). Natural sources of aerosols and their impacts on clouds have been less of a focus than understanding anthropogenic aerosols and their direct and indirect radiative effects (Schmale et al., 2021; Boucher et al., 2013; Sand et al., 2021; Samset, 2022). However, it is challenging to separate the effects on clouds and radiation of anthropogenic and natural aerosols,

and these effects can have opposite signs, including at the poles (Allen & Sherwood, 2011). In addition, cloud-aerosol interactions are non-linear (Gryspeerdt et al., 2019), so estimating anthropogenic impacts on polar clouds requires an accurate understanding of the natural aerosol baseline. Therefore improved representation of natural aerosols and their impacts on clouds are essential for improved anthropogenic climate change estimates.

Sea salt particles resulting from sea spray make up most of the aerosol mass over oceanic regions (Andreae & Rosenfeld, 2008), with an even larger fraction over the polar regions (Sand et al., 2017). Sea spray is composed of a mixture of inorganic salts and an organic fraction (including both dissolved organics and fragments of organic material). In this study, we focus on the inorganic fraction of sea spray emissions and use the wording sea salt aerosols (SSaer) to refer to the inorganic fraction (sodium chloride, sulfate, and other trace salt species) of sea spray. When discussing sea spray we refer to the full mixture of emitted species, which includes both inorganic and organic marine aerosols.

SSaer and sulfate emitted from sea spray can act as Cloud Condensation Nuclei (CCN) (Prank et al., 2022; Xu et al., 2022), and marine organics can act as Ice Nucleating Particles (INP) (Wilson et al., 2015; DeMott et al., 2016). Over polar oceans, sea spray aerosols including SSaer can seasonally make up most of the cloud seeding population (Quinn et al., 2017; Fossum et al., 2018). They also scatter incoming solar shortwave radiation directly (Takemura et al., 2002; Satheesh & Lubin, 2003). In addition, SSaer also change the climate impacts of other species, including anthropogenic pollutants such as nitrate (Chen et al., 2020) and sulfate (Fossum et al., 2020), by regulating their droplet activation. Furthermore, SSaer modulate polar atmospheric chemistry by providing a surface for heterogeneous reactions and leading to bromine activation, with major effects on ozone and mercury depletion events (Hara et al., 2018; Zhu et al., 2019; Marelle et al., 2021). Accurately modeling sea spray aerosols, including inorganic SSaer, is therefore a prerequisite for properly representing the polar atmosphere. In particular, the SSaer physical parameters key to their cloud and radiation interaction and removal processes, are the number flux, the size distribution, and the hygroscopicity.

Sea spray emission over the open ocean is due to wind action that forms bursting bubbles at the sea surface, visible as white caps, which emit aerosols to the atmosphere (Monahan et al., 1986). The sea surface temperature (SST) can also modulate the size and number of aerosols emitted (Mårtensson et al., 2003; Jaeglé et al., 2011; Salter et al., 2015; Liu et al., 2021). Salinity affects the electrolytic properties of water, and as salinity increases, coalescence is inhibited and bubbles form in larger number and smaller radii, which then also affects the emission flux of SSaer (Zinke et al., 2022). There remain significant uncertainties in the open ocean sourced sea spray aerosol emission fluxes, including the relatively well-studied inorganic SSaer, that is emitted into the atmosphere, especially at the cold temperatures in the polar regions. For example, Regayre et al. (2020) found that sea spray emissions in the Southern Ocean needed to be tripled in a global simulation to match observations. Unlike other oceanic areas in the world that remain open throughout the year, estimates of sea spray emissions at the poles depend on a proper representation of sea ice cover, which is still challenging in climate models and exhibits a large spread in model ensembles (Notz & SIMIP Community, 2020; Roach et al., 2020). Additional polar-specific source processes of SSaer include blowing snow over sea ice (Yang et al., 2008; J. Huang & Jaeglé, 2017; Yang et al., 2019; Marelle et al., 2021) and emission fluxes specific to open water leads (Held et al., 2011; Kirpes et al., 2019; Ioannidis et al., 2022). Climate models parameterize emissions from open water leads in sea ice like those from the open ocean, even though wave action and white caps are very different in leads than in open ocean due to e.g., reduced wind fetch, local convection, and the lack of a surf zone on the sea-ice edge (Nilsson et al., 2001). Blowing snow sources of SSaer on the other hand are usually not included in global models and to our knowledge are not included in CMIP6 models.

Due to the ongoing trend of sea ice retreat (Meredith et al., 2019), sea spray emissions at the poles are likely to increase in the coming decades. Specifically, less sea ice means more open ocean and therefore more sea spray (Struthers et al., 2013). In parallel, increased sea spray emissions probably have a negative effective radiative forcing globally (Thornhill et al., 2021), including at the poles (Korhonen et al., 2010; Browse et al., 2014), where it is likely dominated by the aerosol-cloud interaction (Struthers et al., 2011). The cooling induced by SSaer-cloud interactions could partially compensate for the warming caused by sea ice loss. Accurate representation of SSaer in the atmosphere is also important for reliable future climate projections. However, both AeroCom (Sand et al., 2017) and the Coupled Model Intercomparison Project phase 6 (CMIP6) (Mortier et al., 2020; Gliß et al., 2021) reported a large uncertainty in the aerosol budget and seasonality, globally and at the poles. Fanourgakis et al. (2019) also indicated significant model diversity of up to two orders of magnitude in simulated SSAer concentrations over the Southern Ocean, resulting from different parameterizations in global models.

In the present work, we address the following science questions:

1. How diverse are SSaer emissions/concentrations at the poles in CMIP6 models?
2. What are the drivers of this model diversity?
3. How well do the CMIP6 models and ensembles represent SSaer at the poles relative to surface observations and remote sensing?
4. What are the implications of model diversity and changes in SSaer emissions, for the present and future polar climate?

To answer these questions, we conduct an assessment of polar SSaer diversity in CMIP6 models in Section 3.1, by comparing SSaer related variables in the CMIP6 historical experiment. We further evaluate the models against SSaer concentration data from measurement stations and aerosol optical depth from the Moderate-Resolution Imaging Spectroradiometer (MODIS) Aqua and Terra satellite products in Section 3.2. Finally, in Section 3.3 we analyze the historical and future trends of SSaer in the Shared Socioeconomic Pathways 126 and 585 scenarios and the sensitivity of the polar radiative budget to changes in SSaer emissions, through different CMIP6 experiments to shed light on the implications of modeling discrepancies in CMIP6.

2 Materials and Methods

2.1 Models

We use results from 12 climate models that are part of CMIP6. Models were selected based the availability of relevant variables for the evaluation of SSaer. The models included, along with the available variables and source function formulation are indicated in Table 1. Only one additional CMIP6 model features the mass mixing ratio of sea salt aerosol variable (*mmrss*) for the historical experiment (INM-CM5). We have chosen to discard this model because it produces unrealistic SSaer concentrations that are three orders of magnitude larger than any other model. All other CMIP6 models are excluded because they do not provide *mmrss* in the historical experiment.

In order to evaluate the representation polar SSaer within CMIP6 models, we extracted the following from the Earth System Grid Federation (ESGF) platform (ESGF, 2014), for the historical CMIP6 experiment (run with coupled ocean-atmosphere models) and for the period 1951–2014 (as summarized in Table 1): mass mixing ratio of sea salt aerosol (*mmrss*), sea salt aerosol emission flux (*emiss*), sea ice concentration (*siconc*), surface wind speed (*sfcWind*), optical depth of sea salt aerosol at 550 nm (*od550ss*) and planetary boundary layer height (*bldep*). We use this information for all 12 models, but exclude variables that were missing as output on the ESGF platform for certain mod-

els. Future projections are also considered in this work, relying on the Shared Socioeconomic Pathway (SSP) 126 and 585 experiments (ScenarioMIP activity - O'Neill et al. (2016)). The significance, sign and magnitude of trends in these scenarios are calculated using a Mann-Kendall test (Mann, 1945). For the evaluation of SSaer radiative impact, two experiments of the AerChemMIP activity are considered. For that, the top-of-atmosphere net downward radiation flux (*rtmt*) and near-surface air temperature (*tas*) in experiments *piClim*-2x*ss* and *piClim-control* pre-industrial (30 years under 1850 climate) atmospheric composition scenarios are investigated.

For spatial ensemble means, model output is first re-gridded to a common grid, to the lowest model resolution available (2°lon×1.5°lat). The re-gridding is done using Climate Data Operators bilinear remapping tool (Schulzweida et al., 2012). For regionally averaged numbers, a weighted mean is applied, with weights corresponding to the grid cell area. Ground station data usually provide a mass concentration of sodium, whereas models output the SSaer mass mixing ratio. For the comparison between the two, the SSaer mass mixing ratio is therefore converted into a mass concentration under a standard air density at 1 atmosphere and 0°C temperature ($1.2922\,\mathrm{kg\,m^{-3}}$). SSaer in the models is assumed to follow the composition of Seinfeld and Pandis (2016), and sodium mass is thus taken as 30.61% of SSaer mass. Near-surface concentration in the models refers to the concentration within the lowest vertical level. Furthermore, the atmospheric lifetime of SSaer is calculated as the global load (that is, the integral of *mmrss* on the vertical levels for each latitude and longitude) divided by the global emission rate, weighted by grid cell area. We do not use deposition for the the lifetime analysis because it is only available for 8 out of the 12 models. The metrics used to compare models and observations are the normalized mean bias (NMB), defined as NMB=(¡MODEL¿−¡OBS¿)/¡OBS¿, where ¡.¿ is the annual mean, and the Pearson correlation coefficient, simply referred to as correlation (R).

Among the 12 models considered, sea spray emissions are parameterized by 8 different source functions or combinations of source functions (Table 1). The common feature of these source functions is that for a given aerosol radius, the emission flux is proportional to the wind speed raised to a varying exponent. Some of the parameterizations also account for the dependence of sea spray emissions on SST. Although there is still debate on the exact role that SST plays in the sea spray emission process, including it generally improves the fit with observations as reviewed in Grythe et al. (2014). For example, the Jaeglé et al. (2011) parameterization decreases emissions at colder SST, whereas the Salter et al. (2015) source function does the opposite. For polar waters, for example, an increase in SST may decrease the number of sea spray aerosol produced, without significantly affecting the shape of the size distribution (Zábori et al., 2012). This is consistent with the Salter et al. (2015) source function, but opposite to the SST dependence in the Jaeglé et al. (2011) source function, for which emissions increase at higher SST. This shows that not all source functions may be fit for use in polar regions. The source functions are further investigated in Section 3.1.2 based on offline calculations from the source function formulations, using a sectional approach with fixed bins, regardless of what is actually done in the models. This approach is used to evidence the diversity coming from the source functions themselves rather than the aerosol schemes of the models.

To our knowledge, polar-specific sources of SSaer such as blowing snow over sea ice and emissions from leads are not taken into account in CMIP6 climate models, which may limit their performance at high latitudes. Similarly, only the fraction of the ocean that is ice-free can lead to sea spray emissions. Therefore, SSaer emissions at the poles in climate models are highly dependent on a proper representation of sea ice cover. As a consequence, SSaer emissions are probably harder to adequately model at the poles than in any other oceanic region in the world. However, even for mid-latitudes and more generally globally, climate models disagree on SSaer representation, such as their total

emission fluxes, lifetime, burden, and optical properties including hygroscopicity (Burgos et al., 2020; Gliß et al., 2021). The sinks of SSaer such as dry and wet deposition, control their atmospheric quantities. Accurate wet deposition rates require adequate precipitation, which is challenging for Antarctica (Roussel et al., 2020) and the Arctic (Diaconescu et al., 2018) in climate models. In parallel, dry deposition of aerosols is sensitive to the choice of deposition velocity, which is usually not tuned for snow-covered terrain in chemistry-transport models, resulting in large uncertainties in the Arctic (Qi et al., 2017). Dry deposition is also sensitive to boundary layer stability, which is difficult to model especially in polar regions (Holtslag et al., 2013). Finally, the transport of aerosols from the mid-latitudes to the poles can also represent a source of uncertainty in the models. Therefore, it is not expected that climate models would converge in regions as complex as the poles, where in addition to emission fluxes, meteorology (Cai et al., 2021) and anthropogenic aerosol budgets (Sand et al., 2017) are more challenging to represent.

2.1.1 Reanalysis

In order to assess how CMIP6 models compare with more widely used air quality-oriented reanalyses, this work includes two monthly reanalysis products. The Modern-Era Retrospective analysis for Research and Applications, Version 2 (?, ?, MERRA2,)]merra2 and the Copernicus Atmosphere Monitoring Service (?, ?, CAMS,)]inness2019. For the former, the Sea Salt Surface Mass Concentration (*SSSMASS*) variable from the *tavg1_2d_aer_Nx* monthly product is considered, over the period 1980–2021. For the latter, the *CAMS global reanalysis (EAC4) monthly averaged fields* product is used and the three size bins of the *Sea salt aerosol mixing ratio* variable are summed and taken at the first model level, over the period 2003–2021. We also use the monthly climatology of sea ice concentration from the fifth generation ECMWF atmospheric reanalysis of the global climate (?, ?, ERA5,)]era5.

2.2 Observations

2.2.1 Ground based stations

Combining data from the literature (Legrand et al., 2016; Yang et al., 2019) and from the EBAS platform (Norwegian Institute for Air Research, 2022), sodium aerosol concentration measurements were obtained over a multiyear period for 9 stations in the Arctic and 5 in the Antarctic. Their location, the data source, and the period covered by the observations are detailed in Figure 1. When taken from the EBAS platform, the weekly measurements of atmospheric sodium, typically conducted using high-volume air samplers, are then averaged to obtain the annual cycle of monthly means and the related standard deviations, over the entire time period in the data set. We use these observations without assuming a particular cut-off size and directly compare to the total sodium mass derived from the modeled SSaer (maximum radii in the models can be found in Table 1).

The nine Arctic stations include two sites above 80°N (Alert and Villum) in Canada and Greenland, respectively. These two coastal sites are surrounded by sea ice even in summer (blue contour in Figure 1). Data from a third coastal site (Utqiaġvik, Alsaka, 71°N) is available, where, in contrast to Alert and Villum, the shore is sea ice free in summer but sea ice covered in winter. Summit (Greenland) is an inland station in the middle of Greenland. Zeppelin (Svalbard) is a mountainous site (475 m a.s.l.) near the shore of a fjord at 79°N, which is more and more influenced by sea spray (Heslin-Rees et al., 2020). The rest of the Arctic stations considered in this work are in northern Europe (Irafoss in Iceland, Pallas in Finland, Karasjok in Norway and Bredkälen in Sweden). For Antarctica, one of the five stations is far inland (Concordia), one is on the coast of East Antarctica (Dumont d'Urville) and the three others are in coastal western Antarctica (Halley, Neumayer, Palmer). These stations are located between 65°S and 75°S (Figure 1).

2.2.2 Satellite remote sensing

A regional evaluation of SSaer in CMIP6 is conducted by comparing its modeled optical depth with aerosol optical depth (AOD) satellite data from MODIS (Platnick, 2015). To our knowledge, there is no pure satellite climatology for SSaer AOD. Those products available such as MACv2 (Kinne, 2019) usually include a modeled component in their climatology. For the purpose of this CMIP6 model evaluation, a proxy based on MODIS AOD and Angstrom exponent is therefore used to create a simple version of this missing product. A more refined dedicated polar marine AOD climatology product could be created by combining several satellite sources (Dror et al., 2018; Dasarathy et al., 2021; Atmoko & Lin, 2022) in future work. However, the Arctic time series obtained using the methodology described below (Section 3.2.2) is well in line with the SSaer AOD values reported in Xian et al. (2022) for example, which are based on an ensemble of reanalyses. This suggests that the simple proxy used here yields reasonable values of SSaer AOD.

This custom product is based on the MODIS Atmosphere L3 Monthly Products MOD08_M3 (from satellite Terra) and MYD08_M3 (from satellite Aqua) (Platnick, 2015) for the period 2005–2014. The monthly mean AOD at 550 nm is taken from the Dark Target/Deep Blue (DTDB) combined variable *AOD_550_Dark_Target_Deep_Blue_Combined_Mean_Mean*. Then, a filter is applied that aims at keeping only the contribution of SSaer to AOD. This filter is based on the condition that the Angstrom exponent is below 1 to filter out fine-mode aerosols. The implied assumptions are that SSaer are dominated by coarse-mode particles and that coarse-mode aerosols over the polar oceans are dominated by SSaer. The former is shown in e.g. Murphy et al. (2019), the latter assumption is discussed in the next paragraph. The *Aerosol_AE1_Ocean_JHisto_vs_Opt_Depth* variable from MOD08_M3 and MYD08_M3 is used to discriminate Angstrom exponents. It contains, for each month and grid cell, a joint histogram of the calculated Angstrom exponent (0.55–0.86 µm) versus retrieved AOD at 550 nm. This variable provides data only over oceans, and as a result the product we build here is only valid for oceans. We use it as follows: for each grid cell and month, the frequency of records with AE < 1 i.e. $\mathrm{Freq}_{\mathrm{AE}<1} = \mathrm{Counts}_{\mathrm{AE}<1}/\mathrm{Counts}_{\mathrm{AE}}$ is computed, regardless of the AOD joint distribution. The DTDB 550 nm AOD is then multiplied by this $\mathrm{Freq}_{\mathrm{AE}<1}$ factor to approximate the fraction of AOD attributable to coarse-mode aerosols, and by extension SSaer. The resulting estimated fraction of AOD from MODIS attributed to SSaer is referred to as AODss in the continuation. The algorithm created to build this AODss extraction from MODIS is attached to this paper.

The key assumption for the validity of this approach is that coarse-mode aerosols in the MODIS records are dominated by SSaer over polar oceans and therefore that dust has a minor contribution. This hypothesis is supported by the MACv2 aerosol climatology (Kinne, 2019), which provides AOD based on AERONET/MAN and climate models, with species differentiation. We use this data set to evaluate the contribution of SSaer AOD to {SSaer+dust} AOD and assess the validity of the assumption that dust is not an important fraction. In this data set, the fraction of {SSaer+dust} AOD attributed to SSaer is well above 80% over most of the polar oceans, except in coastal areas where important dust sources can be found (Meinander et al., 2022) and the central Arctic, which is permanently covered with sea ice (Figure 1). For these regions, however, AOD in MACv2 is very low and/or dominated by the fine-mode fraction, which is filtered out by our Angstrom exponent criterion. Therefore the MACv2 product supports the assumption that coarse-mode AOD over the polar oceans is essentially SSaer AOD, as illustrated in Figure A1. Sporadic transport events of aerosols (volcanic ash, biomass burning, anthropogenic pollution) can also affect the signal recorded by MODIS, but we argue that such short-lived events are smoothed out by the monthly averaging, except where the number of available records is low.

3 Results and discussion

3.1 Representation of polar SSaer in CMIP6

In the Arctic, the CMIP6 1951–2014 climatology of the SSaer surface mass mixing ratio (referred to as *mmrss* from now on) shows maximum values over the northern Atlantic and northern Pacific (Figure 2), with the mixing ratio decreasing poleward, reaching averages below $1\,\mu g\,kg^{-1}$ in the high Arctic. CNRM-ESM is an exception, with mixing ratios more than one order of magnitude greater than any other model. This discrepancy is discussed later on. The northward negative gradient is consistent with an increase of the relative area fraction covered by sea ice as latitudes increase, which inhibits the production of sea spray. Over the continents, concentrations are generally below $1\,\mu g\,kg^{-1}$, down to less than $50\,ng\,kg^{-1}$ in some models, with *mmrss* decreasing inland, in connection with the deposition of the SSaer during transport. Therefore, all the models have characteristics that are consistent with the expected behavior of SSaer production and transport patterns.

Although the spatial distribution remains relatively consistent (Figure 2), in terms of magnitude, there is a large diversity between models. CNRM-ESM appears as an outlier at both poles, yielding very high *mmrss* of up to $900\,\mu g\,kg^{-1}$, 20 times larger than any other model. This can be explained by a larger coarse size radius of SSaer at emission in CNRM-ESM compared to the other models, as already noted in Thornhill et al. (2021). In this regard, CNRM-ESM being an outlier, this model is not included in the continuation of the analysis unless explicitly mentioned. CNRM-ESM aside, GISS presents the highest mixing ratios, with more than $40\,\mu g\,kg^{-1}$ in the northern Atlantic and more than $1\,\mu g\,kg^{-1}$ over most of the high Arctic and continental areas. At the other end of the spectrum, MRI-ESM and MIROC-ES2L do not exhibit mixing ratios above $10\,\mu g\,kg^{-1}$, and they drop to less than $50\,ng\,kg^{-1}$ over continental areas. This spread in magnitudes will be further analyzed in Section 3.1.2 based on source functions. In some models, the latitudinal gradients are sharper (e.g. BCC-ESM compared to EC-Earth) suggesting different representations of atmospheric dynamics (transport, boundary layer dynamics) and deposition (dry and wet).

For the Antarctic (Figure 3), this climatology of *mmrss* has larger values than for the Arctic, due to the Southern Ocean providing a large source area of sea spray combined with strong winds. A band of maximum *mmrss* is found around 50°S in the Southern Ocean in all the models, followed by a negative gradient toward the pole related to deposition during the transport. Again, CNRM-ESM aside, GISS presents the highest values, whereas MRI-ESM and MIROC-ES2L have the lowest, and the poleward gradient is more or less sharp depending on the model. Similarly to the Arctic, CMIP6 models give a generally consistent spatial distribution of *mmrss* in the Antarctic, except for the magnitudes, which are even more diverse.

The diversity in spatial gradients between models is particularly relevant for the interpretation of ice cores from polar ice sheets (Greenland, Antarctica). Sea salt in ice cores at coastal sites can be used as a proxy for sea ice conditions variability, but models usually show that for continental polar areas, meteorology, atmospheric transport, and deposition control sea salt in ice cores instead (Levine et al., 2014; Rhodes et al., 2018). The differences in transport shown here in CMIP6 models suggest that the relative attribution of sea salt variability in ice cores to transport meteorology and changes in the sea ice source can be quite uncertain. The spatial distribution is consistent from one model to another, but differences in gradient suggest that the representation of atmospheric dynamics and sinks (wet and dry deposition) may differ.

Figure 4 further summarizes the model diversity, including for other SSaer related variables. Similarly to mixing ratios, there is a large diversity in total mass emission and deposition fluxes, which partly accounts for the diversity in *mmrss*. In addition, SSaer

are not found at the same altitudes in all the models. This information is contained in the aerosol layer height, which is defined as a weighted mean of SSaer layer height using the *mmrss* of each layer as the weight (Figure 4). For CESM this height is 956 m, while it is only 136 m in IPSL-CM6. This aerosol layer height is important when it comes to the interaction of SSaer with clouds. The residence time (or lifetime) of SSaer is one of the most diverse metric, with values between a few hours up to several days depending on the model. This factor may explain the differences in transport over land, since models with longer residence time also feature higher concentrations over Antarctica and Greenland (Figures 2 and 3). These differences in lifetime can be explained by the vertical distribution of SSaer: models with longer lifetime also have higher aerosol layer height. GISS is an exception in that case, but the relatively small deposition flux compared to the other models compensates for the lower aerosol height and extends the residence time. SSaer optical depth is also diversely represented in the models, and not directly related to *mmrss*, indicating possible differences in the parameterizations of the size distribution and hygroscopicity. We note that the GISS AOD values for SSaer are much higher than other models, therefore we exclude this model from the AOD analysis that follows.

In summary, there is a large diversity in CMIP6 models in terms of their SSaer climatologies at the poles, from the mass emissions (factor 3 between lower and higher models) to the surface mass mixing ratios (factor 4-5), through the aerosol layer height (factor 7-8), lifetime (factor 9), optical depth (factor 4) and total deposition (factor 2-3). In the Arctic, dry deposition is more diverse (factor 15) than wet deposition (factor 3), whereas in the Antarctic, both dry and wet deposition have a similar inter-model spread (factor 9). This difference in variability in wet deposition might be related to the difficulty to properly reproduce Antarctic precipitation in models (Palerme et al., 2017).

3.1.1 Model diversity drivers

The diversity in SSaer climatology is further investigated and explained in terms of the annual cycle of *mmrss* and the associated drivers (Figure 5). *mmrss* over the ocean is driven by emissions, the height of the boundary layer, and deposition rates. Emissions are themselves driven by wind speed and sea ice fraction. SST also affects emissions, but for consistency this variable is not included in the following analysis on annual cycles of emission drivers, since only four of the models take it into account in their source function. Here the focus is on the dynamical drivers and their effects on emissions and concentrations. Figure 5 presents the annual cycle of the aforementioned variables for the Arctic and Antarctic, averaged over grid points where emissions are strictly positive and the open ocean fraction is at least 10%. This filter is applied to allow a fair comparison across all models.

In the Arctic, mass emissions are consistently at their lowest in the summer months (Figure 5c), when despite increasing sea ice melt and therefore increasing open ocean area (Figure 5e), wind speeds are at their lowest (Figure 5g), thus limiting sea spray. All models show similar magnitudes in summer, except for IPSL-CM6 which features greater values. The spread is larger in the fall/winter months with a factor of up to three between IPSL-CM6 and GISS on the total emission rate in October. This diversity in emissions seems driven mainly by diversity in sea ice (larger spread) and then by wind speed. Furthermore, the source function formulation and size distribution of the emitted aerosols are key factors that are discussed in Section 3.1.2.

For the winter months, when wind speeds are higher, the sea ice fraction seems to be the factor limiting emissions, while in the fall, when there is more open ocean, the wind seems to be the controlling factor. In parallel, the ongoing reduction of sea ice cover in the Arctic appears to be correlated with stronger winds in fall/winter months (Vavrus & Alkama, 2022). Therefore, in the context of future climate, the shape of the annual cycle of emissions is likely to change, with possibly an even greater amplitude between

summer and fall/winter emissions. Given that the radiative impact of SSaer changes with seasons (Section 3.3.1), changes in the seasonality of SSaer emissions might have important implications for the polar climate.

For the Antarctic (Figures 5d, f, h), the emission drivers are even more spread across models, particularly the open ocean fraction in the winter months, resulting in a diversity factor of up to 6 in total mass emissions. Unlike for the Arctic, annual cycles show different shapes in some models. For example, MIROC-ES2L and MPI-ESM show a SSaer production peak in May–Jun whereas the other models have maximum emissions in Mar–Apr, along with a sharper seasonality. In this case, the sea ice cover appears to be the reason for this diversity.

The diversity in emissions is partly translated into *mmrss* (Figure 5a, b) although it does not account for the relative ranking of the models or for some characteristics of the annual cycle. For example, GISS is the model with the lowest mass emissions in the Arctic (Figure 5c), and around median emissions in the Antarctic (Figure 5d), but shows the highest mixing ratios at both poles. This could result from the representation of the dynamics of the boundary layer, since GISS has a mean planetary boundary layer height between 300 to 500 m, about three times lower than other models (Figure 5i, j), which results in a higher boundary layer concentration for the same amount of emissions. EC-Earth also shows very shallow boundary layer heights similar to those of GISS, along with a comparatively higher emission rate at both poles, which should result in mixing ratios higher than in the other models. However, those mixing ratios are lower, due to a shorter lifetime of SSaer of around 14 h, while it is more than a day in GISS (Figure 4). This is also reflected by a deposition flux twice as large in EC-Earth compared to GISS, where the difference mostly comes from dry deposition (Figure 4). In terms of the annual cycle, in the Arctic the seasonality of the boundary layer height shows the same shape as for emissions, which are both consistent across models. Therefore, the cycle of mixing ratio follows the cycle of emissions. However, in the Antarctic, the planetary boundary layer height cycle is more diverse, as is the case for emissions, resulting in more diverse values and seasonality. Deposition fluxes and lifetimes further modify the relative ranking of models in terms of mixing ratio as shown in Figure 4, but the seasonality is not affected.

3.1.2 Role of emission source functions

The source function formulations also affect the diversity in emissions. Figure 6 explores the differences in fluxes resulting from the diversity of source functions used in the CMIP6 models. The source functions and aerosol modes/bins used in the models are summarized in Table 1. All the models except NorESM use a whitecap fraction approach based on surface wind speed, but not all include a dependence on SST. Instead, NorESM uses the air-entrainment-based Salter et al. (2015) formulation.

Figure 6a shows the theoretical mass flux from an offline calculation of SSaer emissions for each source function using an arbitrary fixed wind speed and SST ($10\,\mathrm{m\,s^{-1}}$ and 5°C, respectively) and varying aerosol size bins, as described in Section 2.1. Figure 6b explores the effect on this flux of varying wind speed and SST for given size bins. Some CMIP6 models use a modal aerosol approach, some use a sectional (size bins) aerosol approach. Here, for the sake of comparability of the source functions, we use a sectional approach for the aerosol sizes. Therefore, the following analysis reflects the model diversity due to the source functions without considering the actual aerosol size distributions (modal or sectional) that are included within each model.

Figures 2 and 3 show that CNRM-ESM has *mmrss* much higher than all the other models. This is explained by the use of the Grythe et al. (2014) source function with size bins up to 20 µm radius. First, the other CMIP6 models only emit up to a maximum radius of ∼10 µm, so CNRM-ESM adds an extra mass in the 10 µm–20 µm range. Second,

the Grythe et al. (2014) source function has a coarse emission mode with a mean radius of 30 µm, inducing large emissions of coarse particles which strongly contribute to mass. Figure 6a shows that for a maximum radius of 20 µm, this source function yields a mass flux one order of magnitude greater than any other model for a given wind speed of $10\,\mathrm{m\,s^{-1}}$ and 5°C SST, which is the difference observed in Figure 4.

Figure 6a also shows that for a given choice of aerosol size bins (assuming a sectional approach with mean radii 0.05-0.5-1-R_{max} µm and varying R_{max}), selecting a source function over another can change the flux by up to one order of magnitude (e.g. grey bar for JA11 versus grey bar for GR14). Furthermore, the source functions do not have the same sensitivity to the choice of the larger aerosol size. Some source functions are very sensitive to the radius of the coarser section, which leads to large changes in the mass flux (SM98, MA06 and GR14) with larger mass emissions for bigger particle bins. But for the others, the number flux for larger particles decreases fast which causes the mass flux to increase less as radii increase. For the SSaer emissions, although it is critical for the wind speed (and SST when used) to be accurately represented, the diversity between models is driven primarily by the choice of the source function formulation and aerosol size bins rather than by meteorological differences (see Figure 6a and Figure 6b). When changing wind speeds by $\pm 1\,\mathrm{m\,s^{-1}}$ (which is the spread found in CMIP6 models), the impact on the mass emission flux is generally smaller than a change in the coarse mode aerosol size bins. Figure 6b also shows the influence of accounting for SST in the source function (blue and green stars). In general, changing the SST by ±5°C leads to a similar to smaller change in the mass emission flux than varying the wind speed by $\pm 1\,\mathrm{m\,s^{-1}}$. Since the spread in SST in CMIP6 models is less than 5°C, we therefore conclude that the emission flux dependence on SST is not an important contributor to the CMIP6 model diversity.

The fine aerosol size bins (taken here as 300 nm and smaller aerosol diameter) influence the number of SSaer potentially acting as CCN. BCC-ESM barely produces any SSaer below 300 nm since the smaller aerosol bin considered has a minimum diameter of 200 nm. For the other source functions, we compute the number emission flux considering the following SSaer diameter bins: [30-40-50-60-70-80-90-100-200-300] nm. In this range of diameters, the total number flux of SSaer varies by a factor of 8, except for the MO86 function which yields a number flux 2 orders of magnitude larger in this size range. Therefore, for models including the interactions of aerosols with radiation and clouds, the choice of source function can strongly influence the associated radiative impacts, as illustrated in Prank et al. (2022).

In summary, the large variety in the magnitude of simulated SSaer concentrations at the poles is driven primarily by the choice of aerosol emission sizes and the source function, and secondly by the meteorological drivers of emissions (open ocean fraction, wind speed, mean planetary boundary layer height). The atmospheric processes (deposition, transport, ageing) and thereby the residence time of SSaer drives the differences in spatial distribution and concentrations over the ocean and land. The variety in seasonality is primarily driven by sea ice and meteorology, with diverse sea ice concentration and wind speed annual cycles modulating emissions, but also heterogeneity in the representation of the planetary boundary layer and deposition which influence concentrations irrespective of the emission flux. The choice of aerosol sizes and source function formulation also affects the number of SSaer that could act as CCN.

3.2 Evaluation using observations

3.2.1 Comparison with ground based stations

Given the previously identified diversity in *mmrss* in the investigated CMIP6 models, a comparison with the observed sodium aerosol concentration from ground-based stations is conducted to evaluate individual model and ensemble performance (Figure 7, Fig-

ure 8 and Figure A2). Figure 7 summarizes the comparison between the annual cycle of sodium near-surface concentration in the CMIP6 models and the measurements for the 14 stations. The NMB and correlation of the annual cycle of individual models as well as the ensemble mean are computed. Reanalysis data from MERRA2 and CAMS are also included. The data from observations and models are averaged over the longest available period for each of them, i.e. 1951–2014 for CMIP6, 1980–2021 for MERRA2, 2003–2021 for CAMS, and as indicated in Figure 1 for the measurements.

Arctic

For the Arctic stations, Figure 7 shows that most CMIP6 models have mean concentrations around two to eight times larger than observations. Except for one station where it is negative, the correlation between the modeled and observed annual cycles of concentrations are positive, and mostly above 0.5, indicating a reasonable seasonality. At the Irafoss and Summit stations, the correlation coefficient between the CMIP6 ensemble mean annual cycle and the observations is high, at 0.85 and 0.84, respectively, despite NMB of up to one order of magnitude in individual models. At the Zeppelin, Utqiaġvik, Pallas, Karasjok and Bredkälen stations, NMB and correlations are between 91% and 435%, and 0.61 and 0.81, respectively. Unlike the two previous ones, some models at these four stations are not significantly correlated with the observations at the 95% level. Alert and Villum stations are the only two locations where the NMB is relatively small, and negative (around -20%). However, due to the low correlation (-0.45 at Alert, 0.44 at Villum), this relatively low NMB is not a sign of good performance, as discussed later.

In order to understand if the variation by season for SSaer is correctly represented we apply a bias correction on CMIP6 model output (Figure 8). For each model, the annual cycle is adjusted by the factor ¡OBS¿/¡MODEL¿, which is the annual mean observed sodium concentration divided by the annual mean in the model for each station. Using the bias corrected data (Figure 8) for the Arctic stations Alert and Villum, CMIP6 models have very diverse annual cycles (the median correlation across models is not significant at the 90% level). The ensemble mean has no significant correlation with the corresponding observations at the 95% level (boundaries of the confidence interval have opposite signs). Also, the yearly maximum in Aug–Sep in the models contrasts with observations which are at their minimum during that period. For such high-latitude stations, where the Arctic Ocean is covered with sea ice throughout the year and the production of sea spray does not occur, it is thought that the observed wintertime SSaer maximum originates from blowing snow on sea ice emissions (Yang et al., 2008; J. Huang & Jaeglé, 2017; Yang et al., 2019) or from sea spray originating from leads (Held et al., 2011; Kirpes et al., 2019). In CMIP6 models, these sources are not included in the parameterizations, which may explain the lack of correlation with observations at Alert and Villum and the negative NMB in wintertime. However, some models (UKESM and HadGEM) seem to have the right seasonal cycle at Alert, without including a sea ice source of SSaer. Additional analyses show that the emissions surrounding the location have a minimum in winter, but the annual cycle of planetary boundary layer height varies more with season in UKESM and HadGEM compared to the other models, with higher values in summer and shallower heights in winter (see Figure A3). This explains the shape of the annual cycle despite the absence of winter local sources in the models. Since winter sources such as blowing snow are observed in measurements (Frey et al., 2020), these two models likely have the right annual cycle for the wrong reasons. Except at Utqiaġvik where the Dec–Jan high concentrations are missed by the models, the seasonality is reasonably well captured by the ensemble mean at the other locations.

Antarctic

For Antarctic stations, the magnitudes of the NMB are similar to those of the Arctic sites, except at Dumont d'Urville and Neumayer where several models have a rela-

tive NMB below 100% (Figure 7). The diversity between models is large as well, with no significant across-model correlation at the 90% level for any station, and a strictly positive correlation at the 95% level of the ensemble mean with observations only at Dumont d'Urville and Palmer stations (Figure 8). At Concordia station, two models exhibit an Arctic-like cycle with maximum concentrations in Dec–Feb (MRI-ESM and MIROC-ES2L), while the others produce an annual cycle with maximum concentrations in Jun–Aug. In both groups, the clear maximum recorded by measurements in November is missed.

The models are relatively good at the coastal site of Dumont d'Urville, with a 0.64 correlation and a bias corrected annual cycle mostly within one standard deviation of the observations (Figure 8). In contrast, at Concordia station which is 1200 km further inland from Dumont d'Urville (Figure 1), the correlation with observations is not significant at the 95% level and not one individual model is within one standard deviation of the measurements. This difference in performance might be indicative of inadequate removal processes over land. In particular, climate models at a resolution lower than 1° tend to underestimate precipitation over Antarctica (Tang et al., 2018), which would result in too low wet deposition along transport, and therefore too high concentrations over the continent, despite reasonable concentrations at the coast. In addition, the orography of this region might not be well reproduced in climate models, which could lead to inadequate dynamics and thus explain the shortcomings in CMIP6 in terms of the annual cycle of SSaer.

At Halley station, the comparison is partially hindered by the relatively short length of the observation records, which only cover 3 years and comprise a large variability, but the CMIP6 bias-corrected values are mostly within one standard deviation of the observations for this station (Figure 8). At Neumayer station, the shape of the annual cycle in the models is reasonable but is shifted two months too early compared to measurements. At Dumont d'Urville, all models adequately produce a maximum in Dec–Feb, although generally too high compared to observations and possibly one month late, which leads to a distorted seasonal cycle. A similar comparison can be made for Palmer station, although with a maximum delayed by two months compared to Dumont d'Urville. These two latter stations are the lower latitude ones (north of 70°S) where the sea ice maximum extent in winter is lower according to Figure 1. Like for the Arctic, the absence of a sea ice related SSaer source in the models (blowing snow, leads) degrades their performance during winter.

Reanalyses

Two reanalysis data sets are also included in this analysis (Figure 7) and compared to observations. MERRA2 is known to have a positive bias on SSaer mass concentration of around one order of magnitude even at lower latitudes (Kramer et al., 2020), which was partly attributed to a distortion of the size distribution of SSaer, with too few small particles and too many large ones (Bian et al., 2019). This is consistent with Figure 7 where MERRA2 is found to systematically overestimate concentrations with a larger positive NMB than the CMIP6 ensemble mean, for both poles, between 163% and 2,532%. CAMS has a generally better performance than MERRA2, both in terms of correlation and NMB, the latter being limited to 730% at most. Generally speaking, CAMS is less biased than the CMIP6 ensemble, but has a lower correlation when it comes to reproducing the observed annual cycle. These two comparisons show that despite being commonly used as validation data sets, reanalyses have difficulties in reproducing observed SSaer concentrations at the poles, and have a generally poorer performance than the CMIP6 ensemble. However, since SSaer concentrations are not assimilated in these reanalyses, and AOD is assimilated only as total AOD, a better performance than CMIP6 was not expected.

3.2.2 Comparison of modeled SSaer AOD with MODIS AODss

AOD is often used to evaluate aerosols in climate models, since it is closely related to the full aerosol burden throughout the atmospheric column, including the impact of water uptake on aerosols. It is also more closely related to direct aerosol-radiation climate forcing than surface observations, and is less sensitive to errors in vertical aerosol distributions. SSaer AOD at 550 nm is provided for a subset of CMIP6 models including BCC-ESM, EC-Earth, IPSL-CM6, MPI-ESM, MRI-ESM, NorESM, and compared here to AODss at 550 nm extracted from MODIS Dark Target/Deep Blue satellite data (Figure 9). The monthly MODIS data are processed as described in Section 2.2.2 to approximate the contribution of SSaer to total AOD, noting that AOD is not available for cloud covered regions and ice/snow covered surfaces. MODIS data is also scarce during the polar night due to the absence of visible light. MODIS Terra and MODIS Aqua AODss are shown separately due to the differences between these two monthly AOD products (Sogacheva et al., 2020).

Figure 9 shows the magnitudes and spatial patterns of SSaer AOD in CMIP6 and AODss in MODIS, for the Arctic and the Southern Ocean. In the northern Atlantic, the CMIP6 ensemble median is around 0.02 (0.04, respectively) higher than MODIS Terra (Aqua, respectively). Spurious high AODss values in satellite data over the high Arctic (brown pixels in Figure 9 middle with AODss up to 1 on average) could be artifacts related to the scarcity of valid records available in the region (due to possible cloud contamination or poor snow/sea ice screening) making the comparison more difficult. For the Antarctic, values south of 60°S are comparable between CMIP6 SSaer AOD and MODIS AODss, below 0.02 in coastal regions with a positive northward gradient up to around 0.08 at 60°S. However, in the area between 50°S and 60°S, the band of maximum SSaer AOD in CMIP6 is not observed in the AODss MODIS data (Terra or Aqua), except for sporadic hot spots. For this area, the spatial distribution in MODIS is less homogeneous and has a lower AODss on average compared to CMIP6. Given the semi-permanent presence of clouds at these latitudes, around 90% annually (Lachlan-Cope, 2010), a sampling bias in the MODIS data cannot be excluded to account for this discrepancy, which does not invalidate the high values in CMIP6.

The spatially averaged SSaer AOD and AODss show reasonable agreement between CMIP6 and MODIS in terms of the annual cycle (Figure 9 right). For the Arctic, MODIS features a late winter (Feb–Mar) maximum in AODss that is not represented in the models, whereas most models have a maximum SSaer AOD in early winter (Dec–Jan) that is not found in MODIS and up to 0.1 higher than the MODIS values. However, for those winter months (Nov–Feb), the MODIS data are more sparse than in summer (Jun–Sep), which could result in another sampling bias (Figure 9 right - grey bars). Since cloud cover is lower in winter compared to summer (Eastman & Warren, 2010), and should therefore impede AOD retrieval less often, sea ice cover can explain the lack of records, in combination with the polar night. Sea ice is at its maximum extent and is too bright a surface for MODIS instruments to accurately separate the contribution to back-scattering from the ground and from aerosols (Mei et al., 2013), leading to fewer valid records in winter than in summer. On the other hand, the MODIS-derived annual cycle of AODss is quite similar to the cycle of total aerosol mass and surface area observed in Tunved et al. (2013), which could indicate limitations in our AODss extraction approach. Similarly, the scarcity of MODIS data in the Antarctic for Mar–Sep prevents such a comparison. Furthermore, the observed decrease in AODss in Apr–May could be due to a sampling bias, since MODIS records are less numerous south of 60°S compared to other months (Figure 9 - grey bars). For the austral summer months (Nov–Feb), when the comparison is less uncertain due to a larger number of available records, all the models are within one standard deviation of both MODIS Terra and Aqua values and closer to the Aqua mean. This is true for all the models in the Arctic, and most of them in the Antarc-

tic. The shape of the monthly variations is reasonably well reproduced in both cases, except in winter.

The CMIP6 ensemble is closer to MODIS Terra when it comes to climatological maps, but closer to MODIS Aqua for the summer months, when the comparison is more robust thanks to a larger number of MODIS records. The offset of around 0.02 obtained here between MODIS Aqua and MODIS Terra in our AODss product is well known and described in the literature, in which MODIS Aqua is considered to be more accurate than MODIS Terra (Sogacheva et al., 2020). Therefore, the better agreement of CMIP6 models with MODIS Aqua in summer is an indication that the SSaer AOD is reasonably captured in the CMIP6 models, although the model variability is large for the winter months.

Despite the fairly large discrepancies in *mmrss* revealed in Section 3.2.1, the SSaer AOD at 550 nm shows better performance in the CMIP6 models compared to the satellite data. This indicates that the direct radiative effect of SSaer is likely well reproduced for the poles as well. This also suggests, given the bias on surface mass concentrations, that (i) the size distribution of SSaer might not be adequate, possibly steered toward too coarse particles, or (ii) that the vertical distribution of SSaer is biased and accumulates too much mass at the surface. However, the good performance in SSaer AOD is not necessarily a sign of adequate fine mode number concentrations. Some models are known to have hygroscopic growth factors that are too high (Burgos et al., 2020), which can increase SSaer AOD despite incorrect (too low) quantities of fine fraction mode particles. Although this is not analyzed further in this work, compensating effects between number, size and hygroscopicity of SSaer needs further investigation in the future.

3.3 Implications for our understanding of polar climate

In this section we address the implications of the diverse representation of SSaer in CMIP6 for our understanding of present and future climate. In what follows, we first evaluate the sensitivity of the polar climate to SSaer based on the CMIP6 *piClim*-2x*ss* experiment. Then, historical and future trends of SSaer emissions and *mmrss* are investigated under scenarios SSP126 and SSP585 to assess the uncertainty borne by climate projections owing to SSaer.

3.3.1 Radiative impact of SSaer

The pre-industrial climate experiments from the AerChemMIP activity provide a control (*piClim-control*) and a doubled SSaer emission (*piClim*-2x*ss*) experiment, for a 30 year period under 1850 climate conditions. Three CMIP6 models provide the top-of-the-atmosphere net downward radiative flux (*rtmt*) for these experiments and are used in this section. The change in *rtmt* between the 2x*ss* and *control* experiments is used here to evaluate the radiative impact of SSaer. The entire 30 year period is considered. For the three models considered, this includes the aerosol-radiation interaction and the aerosol-cloud interaction, although they cannot be disentangled, since *rtmt* provides total radiation only (short-wave + long-wave). The *piClim* simulations are fixed-sst, so that *rtmt* includes the effect of rapid atmospheric adjustments, but not the effect of climate feedbacks from long-term surface temperature change. In this respect, the *rtmt* change is comparable to an effective radiative forcing.

One important factor for the direct and indirect radiative effects of SSaer is their vertical distribution. We show the diversity in the vertical distribution of both SSaer and clouds in Figure A4 for ocean/ice covered regions north/south of 60°N/S. There is a large diversity between modeled profiles, of more than two orders of magnitude above 5,000 m altitude for SSaer, and a factor of around 10 in clouds throughout the column. This suggests that the radiative impact of SSaer can also be assumed to be very diverse and uncertain.

Figure 10 shows the average change in *rtmt* between the doubled SSaer emissions and the control experiment, for summer months and winter months in the Arctic and Antarctic. In summer, when sea ice extent is at its minimum in the Antarctic, the radiative impact of SSaer is mostly negative (cooling effect) in the three models over the ocean, with up to -10 $\mathrm{W\,m^{-2}}$ in NorESM and -5 $\mathrm{W\,m^{-2}}$ in IPSL-CM6 and UKESM (Figure 10). This important change is probably partly related to the aerosol-cloud interaction and its albedo effect over darker surfaces (open ocean), as found in Struthers et al. (2011). The aerosol direct effect also likely contributes to this change, especially in NorESM where the change in AOD is large over the Southern Ocean, with more than +0.25 on average (Figure A5). Such an important change is not found in the other models for the Southern Ocean (less than +0.1), explaining why the cooling effect is larger in NorESM in summer in the Antarctic than in IPSL-CM6 and UKESM.

Over the Antarctic continent in summer, for most areas the radiative impact cannot be significantly distinguished from zero at the 90% level according to a Wilcoxon test, but regionally averaged south of 60°S, a negative radiative impact significant at the 95% level is found, comprised between -0.34±0.02 $\mathrm{W\,m^{-2}}$ and -1.01±0.07 $\mathrm{W\,m^{-2}}$ (Table 2). In winter, when sea ice extent is larger and there are fewer areas prone to sea spray production in the region, the radiative impact is slightly positive in West Antarctica but mostly not significantly different from zero at the 90% level in the region when considering all three models (Figure 10 and Table 2).

NorESM and UKESM indicate a cooling effect in the high Arctic in winter, with a regionally significant negative radiative impact at the 95% level (Table2). IPSL-CM6 suggests a small heating effect in northeastern Canada and a slight heating in the high Arctic for Dec–Feb, although the regional average is smaller than the cooling obtained in the other models. In summer, the changes are stronger and more heterogeneous, with regions of large cooling next to regions of large heating, although generally not significant at the 90% level (Figure 10), resulting in a regionally weak cooling effect overall in all the models (Table 2). The weak change in AOD in summer can partially explain this moderate radiative effect (Figure A5).

The effects of doubling SSaer can be further described in terms of changes in air surface temperature (*tas* variable in CMIP6), as shown in Figure A6. NorESM predicts a warming in the winter both in the Arctic and Antarctic (+0.20°C and +0.17°C, respectively), while the response in the other models is either a slight cooling or warming, but one order of magnitude smaller. In the summer, models agree on a cooling effect in the Arctic (-0.013°C to -0.078°C), while the sign of the change is uncertain in the Antarctic (the average of the three models shows a zero net change). In the winter, these changes in temperature are equally driven by oceanic and land regions, whereas in the summer the temperature change is mainly found above land. This may be related to the more homogeneous surface albedo in winter when sea ice extent is large and land is covered in snow, whereas in summer the heat capacity of the open ocean contrasts with that of the land. These changes in surface temperature are not directly connected to the changes in top-of-the-atmosphere radiation found in Table 2, particularly in the Antarctic where the large summer decrease in radiation in NorESM (-1.01 $\mathrm{W\,m^{-2}}$) yields a surface warming of +0.065°C. Cooling/heating effects over land/ocean which have different heat capacity and albedo may be at play in this case. The vertical distribution of the changes in radiation may also play a role.

Figure A6 also shows the same change in surface temperature but in the *piClim-2x**dust*** experiment, where dust emissions are doubled, instead of SSaer. In the Antarctic, both species have similar impacts on surface air temperature (very limited in summer months, slight warming in winter months, on average). In the Arctic, dust have a cooling effect in winter, of the same magnitude as the warming induced by SSaer, whereas in summer, the cooling from SSaer is one order of magnitude larger than the cooling from dust. The changes are also more widespread around zero in the case of SSaer, with wider

distributions than for dust, suggesting a greater sensitivity to SSaer than dust. Compared to SSaer, dust has limited local sources at the poles and mostly comes from long-range transport, which explains its smaller regional impact. However, this comparison speaks to the relevance of evaluating more closely SSaer and their climate impacts at the poles, which are comparatively less studied than for dust.

The implications of the previous analyses are not straightforward, since the *piClim* experiments consider pre-industrial atmospheric conditions, free of the current anthropogenic background. Although polar regions remain relatively pristine areas, they are affected by the transport of anthropogenic emissions from lower latitudes through warm air mass intrusions (Li & Barrie, 1993; Quinn et al., 2002; Dada et al., 2022). The non-linearity of aerosol-cloud interactions (Gryspeerdt et al., 2019) requires an adequate aerosol background, including anthropogenic sources, to obtain reasonable estimates of the indirect effect of SSaer emissions and therefore its radiative impact. Furthermore, the radiative impact depends not only on the proper representation of the number and sizes of SSaer, but also on their hygroscopicity, particularly for the direct effect (Zieger et al., 2017), which are quite uncertain according to Section 3.1.

The relatively strong effect on radiation of doubled SSaer emissions puts Figures 2, 3 and 5 into perspective: the difference in SSaer emissions between two models can be up to a factor of 4, which according to Figure 10 should mean that the resulting radiative budget at the poles could differ by up to $2\,\mathrm{W\,m^{-2}}$ (depending on the season and the model). This suggests that the uncertainty on the polar radiative budget related to SSaer within CMIP6 models could have the same magnitude as the 20^{th} century increase in global radiative forcing (Myhre et al., 2013). These numbers are in line with those from Struthers et al. (2011), where a 23% increase in SSaer AOD in the Arctic is estimated to result in a -0.2 to $-0.4\,\mathrm{W\,m^{-2}}$ radiative impact.

3.3.2 Historical and future trends

As a result of polar amplification, the polar climate is changing even more dramatically than the global climate. Given the connection of sea spray emissions with sea ice and atmospheric dynamics (e.g. wind speed), significant trends can be anticipated in SSaer both in present day and future scenarios. These are investigated using ScenarioMIP experiments SSP126 and SSP585 (O'Neill et al., 2016). The analysis conducted hereafter is restricted to the six CMIP6 models that provide *mmrss* in both scenarios, namely GISS, HadGEM, MIROC-ES2L, MRI-ESM, NorESM and UKESM. We note that observations do not have long enough time series to compute multidecadal trends for validation purposes.

In the historical period 1951–2014, the mass emission flux of SSaer in the polar regions generally increased and comparatively more homogeneously in the Southern Ocean than in the Arctic (Figure 11 top). In the latter region, emissions increased more strongly in the Barents Sea and Greenland Sea, at a rate of up to +6% per decade. In the high Arctic, this trend is lower, between +1.5% and +3% per decade, with no trend between -60°E and -180°E. In the Southern Ocean the increasing trend is more homogeneous, between +1.5 and +6% per decade in most of the area. For the Arctic and Antarctic, the historical trend is mainly driven by sea ice retreat, although a slight increase in wind speed is also found in the Antarctic (Figure A7). This Antarctic increase in SSaer is consistent with the findings of Korhonen et al. (2010). To some extent, the difference in trends of wind speed between the Arctic and Antarctic might be related to an asymmetry in the trends and dynamics of stratospheric ozone depletion (Turner et al., 2009).

Future scenarios in CMIP6 follow the Shared Socioeconomic Pathway (SSP) trajectories (O'Neill et al., 2016). Here, we consider the two extreme scenarios, SSP126 and SSP585. SSP126 represents the low end of the range of plausible future pathways, where radiative forcing reaches a level of approximately $2.6\,\mathrm{W\,m^{-2}}$ in 2100 compared to the pre-

industrial period. SSP585 is at the other end of the spectrum, with a radiative forcing of approximately 8.5 $\mathrm{W\,m^{-2}}$ at the end of the century. In both of these scenarios, the Arctic surface air temperature warms more than the global mean. The change in temperature between 2000–2014 and 2085–2100 is different by a factor of around 2 between the global and Arctic average (3.8°C versus 1.5°C in SSP126 and 10.8°C versus 5.1°C in SSP585, respectively), and with a large uncertainty (model spread of 7°C in SSP126 and 10°C in SSP585). In contrast, the Antarctic has a lower warming than the global mean in both scenarios (Table A1).

The spatially averaged time series of the yearly surface *mmrss* (Figure 11) show different behaviors between the two poles over the historical period and in the two future scenarios SSP126 and SSP585. In the Arctic, in scenario SSP585, each individual model features an increasing trend resulting in the multiplication of surface *mmrss* by a factor of 1.75 to 2.8 in 2099 compared to the 1951–1971 average (hereafter referred to as baseline). In the ensemble mean, this increase is by a factor of 2.2. In the SSP126 scenario, three models show a stabilization after 2050 and a slight decrease at the end of the century. The two remaining models feature a stronger increase, lasting until the end of the century and reaching levels comparable to those obtained in some models in SSP585. The associated ensemble mean stabilizes at just under a 1.5 increase at mid-century compared to the baseline. These trends mirror the trends in Arctic sea ice in the CMIP6 models analyzed in Notz and SIMIP Community (2020), showing decreasing sea ice cover until 2050, followed by a stabilization in SSP126 and a continuous decrease until the end of the century in SSP585. As a result, differences in trends in individual models might come from differences in their underlying sea ice evolution. In the Antarctic, the SSP585 trajectory is similar to that in the Arctic, except for a smoother increase, by no more than a factor of 2 in the more extreme model. Contrary to the Arctic, the increasing trend in *mmrss* starts in the 1980s, and the SSP126 and SSP585 trajectories start separating only around the year 2030, after which *mmrss* reaches a plateau in SSP126 until the end of the century. For both poles, NorESM, which is the only model in this analysis that includes an SST dependence in its sea spray source function, and which is not based on a whitecap approach, shows the smallest increase in concentration at the end of the century, in SSP126 and SSP585. This is consistent with Figure 6 which showed that for increased SST, the SSaer mass flux decreases in the SA15 source function. As a result, in a warming climate, accounting for the increase in SST decreases the SSaer mass flux at the poles compared to not accounting for it. Generally speaking, the trends in all the models are marginally larger in winter than in summer. For comparison, mid-latitude oceans do not show historical or future trends in *mmrss*.

In addition to following different trajectories, future trends in surface *mmrss* in the Arctic and Antarctic also have a different spatial distribution, although in both cases a slight negative trend is found over land in Greenland and the Antarctic continent (Figure A8). This negative trend over land can be explained by increasing precipitation, and therefore decreased aerosol residence time, in SSP scenarios in the Arctic (McCrystall et al., 2021) and over Antarctica (Tewari et al., 2022). All of the Arctic Ocean where sea ice can currently be found features a strong decreasing trend in sea ice concentration (Figure A8), which explains the strong increasing trend in *mmrss* in scenario SSP585. In contrast, the trend in the Antarctic is mainly driven by increasing *mmrss* in the Bellingshausen Sea, and marginally by localized spots in the Wedell Sea, which appear to be sea ice driven (Figure A8).

A multiplication of SSaer mass emissions in the Arctic by 3 in SSP585 (as indicated by the CMIP6 ensemble mean) could imply a regionally negative radiative impact of around -1 $\mathrm{W\,m^{-2}}$ to -2 $\mathrm{W\,m^{-2}}$ in winter at the end of the century based on Section 3.3.1 (see Figure 10 and Table 2). In particular, UKESM that showed a high sensitivity to doubled SSaer emissions (Table 2) is also the model with the largest future trends in scenario SSP585. The limited emission trend in the Antarctic, including in SSP585, sug-

gests a smaller counteracting effect of SSaer on polar warming. Nevertheless, these changes in mass emissions do not necessarily translate into a similar change in number of SSaer, and the latter can have a large impact on the indirect effect of SSaer. No information on the change in number of aerosols is available in CMIP6 models to further investigate these future trends in radiative effect, making them quite uncertain.

4 Conclusions and Perspectives

This work evaluates the representation of SSaer in polar regions within CMIP6 including a comparison to surface station observations and satellite AOD. Implications for the radiative balance at the poles in the present-day and future climate are also investigated. We address the questions:

How diverse are SSaer emissions/concentrations at the poles in CMIP6 models? The inter-model comparisons result in the same conclusions for the Arctic and Antarctic, with a large diversity (up to a factor of 5) in the magnitude of simulated surface mass concentration of SSaer. The spatial distribution is generally consistent between models although the amount of SSaer transported over land varies. Diversity is also important in emissions (factor 3), aerosol layer height (factor 7-8), lifetime (factor 9), optical depth (factor 4) and total deposition (factor 2-3), resulting in a generally uncertain SSaer budget at the poles in CMIP6.

What are the drivers of this model diversity The model diversity in CMIP6 is driven by differences in the sea spray source function formulations and by the drivers of sea spray emission (wind speed, sea-ice cover). We also show large differences in residence time which affect the transport of SSaer and are responsible for model diversity over land. Other SSaer related variables such as AOD, aerosol layer height and deposition fluxes are also diversely represented. We show that even if the emissions were identical, the surface mixing ratio of SSaer would still be different due to different treatments of boundary layer dynamics, aerosol models (micro-physics, treatment internal/external mixing, hygroscopicity, size bins/modes), and deposition fluxes of the SSaer.

How well do the CMIP6 models represent SSaer at the poles relative to surface observations and remote sensing? The evaluation of the modeled surface concentrations of sodium mass against ground station observations shows there is a large positive bias of up to one order of magnitude in CMIP6 models. Once the mean bias is corrected, the seasonal variations of SSaer concentration are relatively well captured for lower-latitude stations. For high-latitude stations, there is a deformation of the annual cycle in models compared to observations. The absence of wintertime local sources of SSaer such as blowing snow over sea ice and emissions from open leads can be one reason for that. Possible biases in sea ice representation could also be responsible. Models that include a SST dependence in the SSAer source function are not less biased than ones that do not, because the effect of SST change is smaller than other sources of bias from source functions, meteorological drivers, and aerosol processing. Modeled SSaer AOD compares well with satellite data, potentially indicating that improvements could be made to the size distributions to overcome the discrepancy in concentrations, assuming that the hygroscopicity factor is adequately represented.

What are the implications of model diversity and changes in SSaer emissions, for the present and future polar climate? Pre-industrial and future climate CMIP6 experiments show that models agree that a doubling of SSaer emissions exerts a net negative radiative perturbation at the top of the atmosphere in summer in the Arctic and the Antarctic, with less agreement for the sign of the impact in winter. In terms of surface temperature, models agree on a cooling effect in summer in the Arctic but disagree on the sign of the change for winter and for the Antarctic. These impacts are generally heterogeneous in terms of their spatial distribution, but the large uncertainty in the present-day

emissions shown here means possibly an uncertainty of up to $2\,\mathrm{W\,m^{-2}}$ in the polar radiative budget. A multiplication of SSaer mass emissions in the Arctic by more than 2 in SSP585 (as indicated by the CMIP6 ensemble mean) could imply a regionally negative radiative impact around -1 $\mathrm{W\,m^{-2}}$ in winter at the end of the century.

These conclusions highlight the need for additional research on the representation of SSaer at the poles. In particular, polar-specific source functions and size distribution could help improve the simulated concentrations according to our findings. Additionally, this work shows that aerosol-radiation and aerosol-cloud interactions of SSaer at the poles cannot be ignored in models and need to be activated and accurately represented to obtain a reliable radiative budget, including to quantify anthropogenic aerosol radiative effects.

Tables

Table 1. CMIP6 models considered and their sea spray source function and emission drivers. MA06 is (Mahowald et al., 2006), MO86 is (Monahan et al., 1986), MA03 is (Mårtensson et al., 2003), JA11 is (Jaeglé et al., 2011), GR14 is (Grythe et al., 2014), GO03 is (Gong, 2003), SA15 is (Salter et al., 2015), and SM98 is (M. H. Smith & Harrison, 1998). For the limit radii of sea salt aerosols, values in italic indicate smallest/largest lognormal modes instead of cut-off sizes.

Model	**Source function**	**Drivers**	**Limit radii (µm)**	**Data used**						
				mmrss, siconc, sfcWind	*emiss*	*od550ss*	*bldep*	*dryss/wetss*	*piClim*	*SSP*
BCC-ESM	MA06	Wind	0.1-10	x		x				
CESM	MO86, MA03	Wind, SST	0.02-10	x	x		x	x		
CNRM-ESM	JA11, GR14	Wind, SST	0.03-20	x						
EC-Earth	GO03, SA15	Wind, SST	*0.09-0.794*	x	x	x	x	x		
GISS	MO86	Wind	0.1-4	x	x		x	x		x
HadGEM	GO03	Wind	0.05-5	x	x		x			x
IPSL-CM6A	MO86, SM98	Wind	*0.1-1.185*	x	x	x	x	x	x	
MIROC-ES2L	MO86	Wind	0.1-10	x	x		x	x		x
MPI-ESM	MO86, SM98	Wind	*0.5*	x	x	x	x	x		
MRI-ESM	MO86	Wind	*0.13-1.75*	x	x	x		x		x
NorESM	SA15	Wind, SST	*0.0475-0.75*	x	x	x	x	x	x	x
UKESM	GO03	Wind	0.05-5	x	x		x		x	x

Full model names and CMIP6 references

The Beijing Climate Center Earth System Model (Wu et al., 2020) – BCC-ESM1
The Community Earth System Model (Danabasoglu et al., 2020) – CESM2
The Centre National de Recherches Météorologiques Earth System Model (Séférian et al., 2019) – CNRM-ESM2-1
The European Community Earth System Model (Döscher et al., 2022) – EC-Earth3-AerChem
The NASA Goddard Institute for Space Studies Earth System Model (Miller et al., 2021) – GISS-E2-1-H
The Hadley Centre Global Environmental Model (Sellar et al., 2020) – HadGEM3-GC31-LL
The Institut Pierre Simon Laplace Climate Model (Boucher et al., 2020) – IPSL-CM6A-LR-INCA
The Model for Interdisciplinary Research on Climate Earth System for Long-term simulations (Hajima et al., 2020) – MIROC-ES2L
The Max Planck Institute Earth System Model (Gutjahr et al., 2019) – MPI-ESM-1-2-HAM
The Meteorological Research Institute Earth System Model (Yukimoto et al., 2019) – MRI-ESM2-0
The Norwegian Earth System Model (Seland et al., 2020) – NorESM2-LM
The UK Earth System Model (Sellar et al., 2020) – UKESM1-0-LL

Table 2. Regionally averaged mean change in top-of-the-atmosphere net downward radiation between the *piClim*-2x*ss* and *piClim-control* scenario. ± indicate 95% confidence intervals. Bold values indicate that the radiative impact is significant at the 95% level according to a Wilcoxon test. Arctic is all grid points north of 60°N and Antarctic is all grid points south of 60°S.

	Arctic		**Antarctic**	
	Dec–Feb	Jun–Aug	Jun–Aug	Dec–Feb
IPSL-CM6	**0.17±0.01**	**-0.48±0.03**	0.01±0.008	**-0.34±0.02**
NorESM	**-0.61±0.01**	**-0.29±0.04**	**-0.12±0.01**	**-1.01±0.07**
UKESM	**-0.33±0.01**	**-0.24±0.01**	**0.09±0.005**	**-0.37±0.02**

Figures

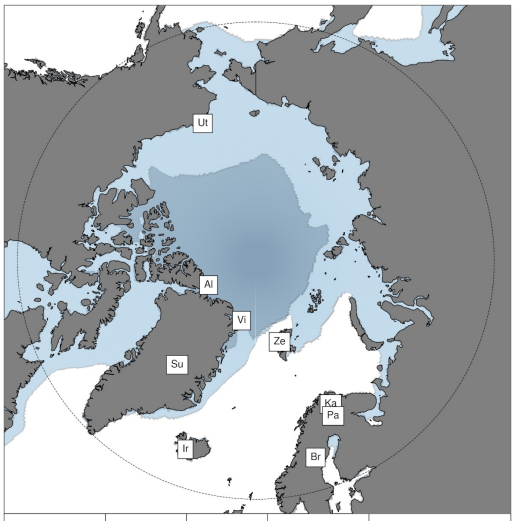

Station	Lat	Lon	Period	Source
Irafoss	64.08	-21.01	2006-2020	EBAS
Bredkalen	63.85	15.33	2009-2020	EBAS
Karasjok	69.46	25.21	2001-2010	EBAS
Pallas	68.0	24.23	2003-2019	EBAS
Zeppelin	79.0	12.0	1993-2020	EBAS
Villum	81.6	-16.67	2000-2021	EBAS
Alert	82.49	-62.34	1980-1990	Yang et al., 2019
Utqiaġvik	71.32	-156.61	1984-2001	Yang et al., 2019
Summit	72.58	-38.48	2003-2006	Yang et al., 2019

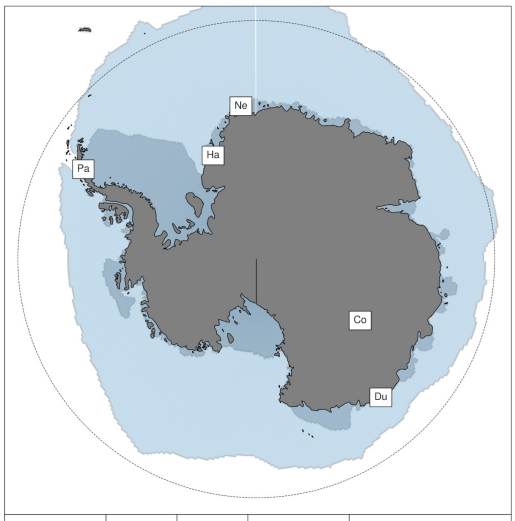

Station	Lat	Lon	Period	Source
Neumayer	-70.66	-8.26	1983-2007	Yang et al., 2019
Halley	-75.6	-26.21	1991-1993	Yang et al., 2019
Concordia	-75.09	123.33	1990-1998	Yang et al., 2019
Dumont d'U.	-66.67	140.0	1991-2013	Legrand et al., 2016
Palmer	-64.77	-64.05	1990-1996	Yang et al., 2019

Figure 1. Arctic and Antarctic measurement stations providing sea salt surface mass concentration data. Blue colormaps indicate areas with a sea ice concentration above 50%. The lighter blue is for February in the Arctic, and August in the Antarctic. The darker blue is the opposite. The sea ice data are from ERA5. The black dashed line shows the 60° limit considered for regional aggregated analyses. Abbreviations in the maps are the first two letters of the corresponding station name.

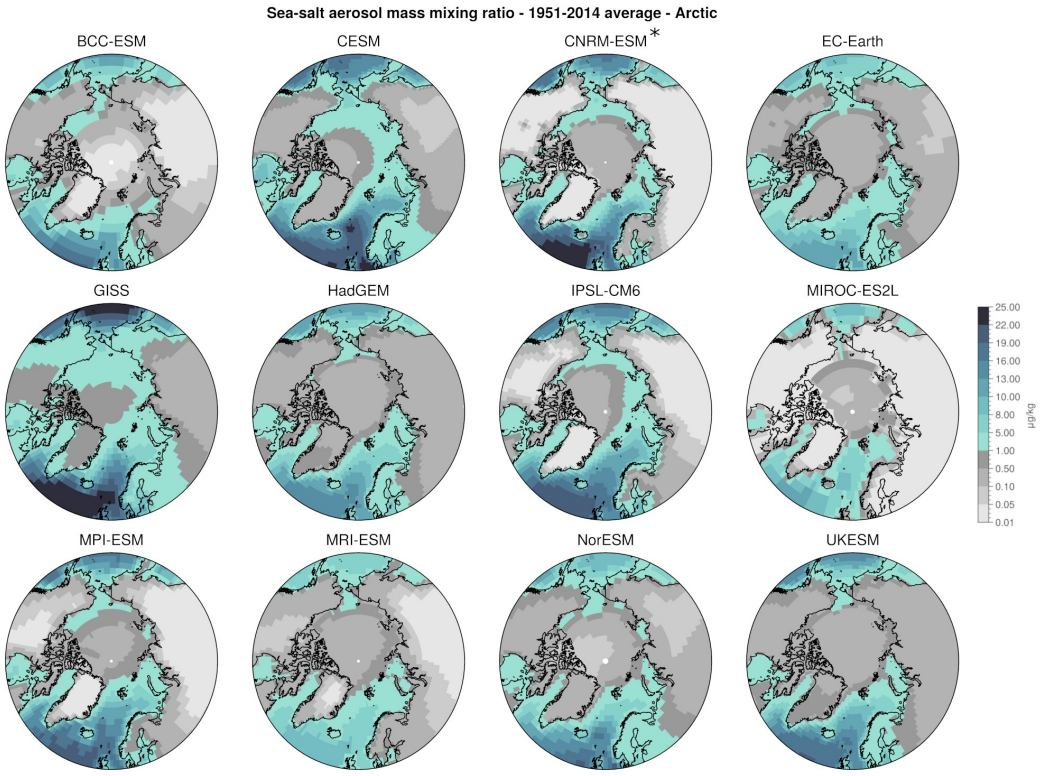

Figure 2. Sea salt aerosol mass mixing ratio in the lowest model level. Annual average for the period 1951–2014 in the CMIP6 historical scenario. Arctic map. NB: CNRM-ESM values are divided by 25 to fit in the colorbar.

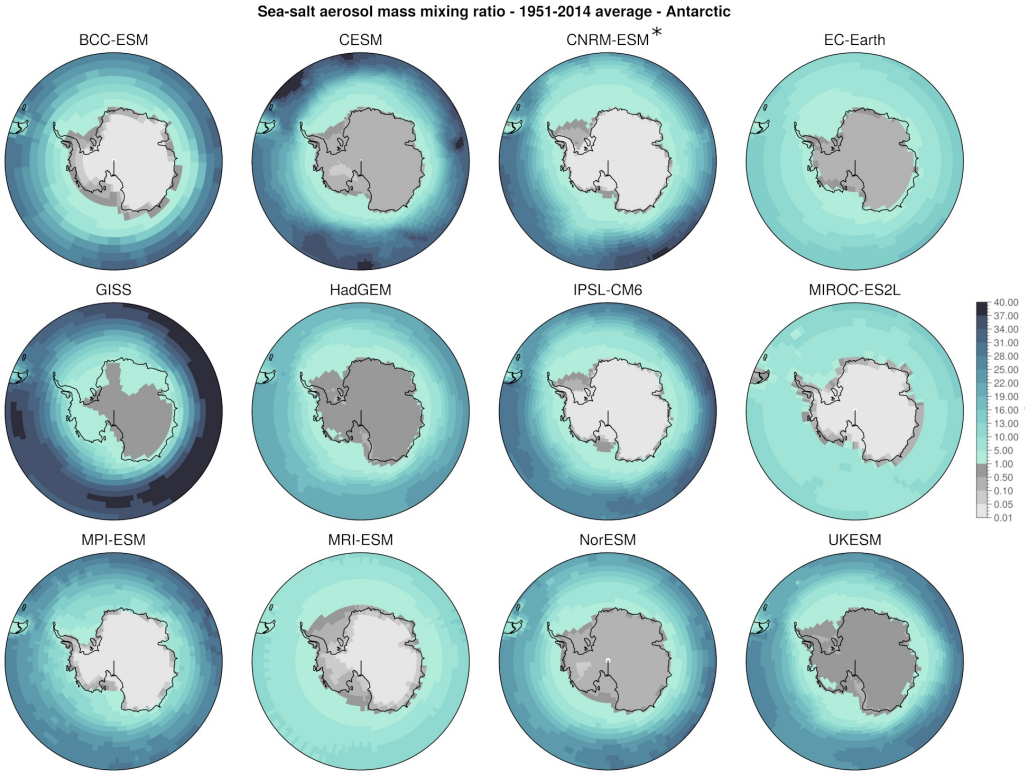

Figure 3. Same as Figure 2 but for the Antarctic.

Figure 4. Model diversity in mass emissions, surface mass mixing ratio, aerosol layer height, AOD, dry and wet deposition, and lifetime of sea salt aerosol. Average for the period 1951–2014. The color scale highlights the highest values for each column. CNRM-ESM is excluded from this color scale for mass emission and *mmrss*. Empty cells indicate that values are not provided by the model. *mmrss* is multiplied by 10 and AOD is multiplied by 1000 for improved readability.

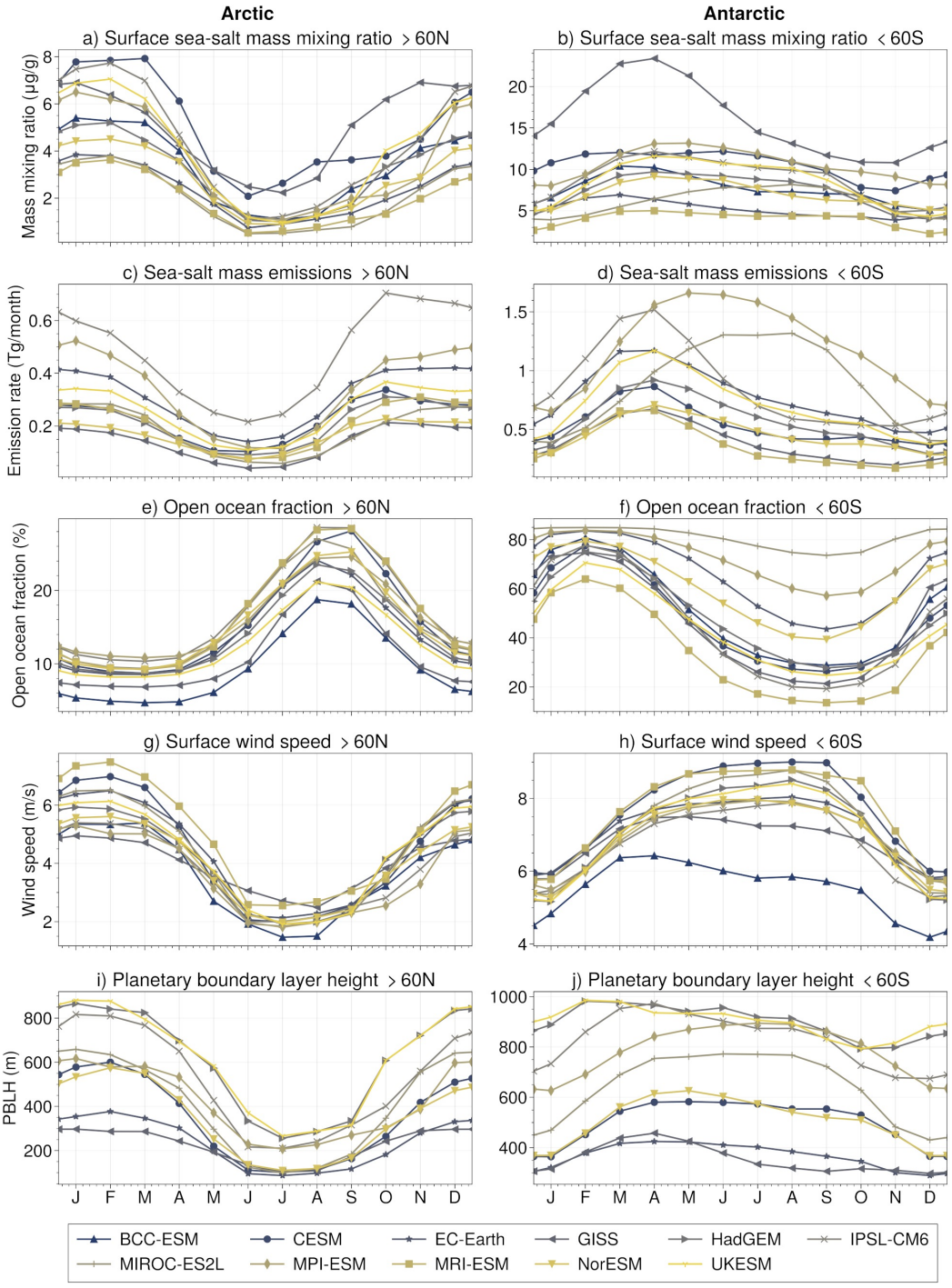

Figure 5. Annual cycles of sea salt aerosol mass mixing ratio at surface level (a,b), sea salt aerosol mass emission (c,d), fraction of open ocean (e,f), surface wind speed (g,h) and planetary boundary layer height (i,j) at latitudes above 60°N (left) and below 60°S (right) in CMIP6 models for the period 1951–2014. Lines show the monthly average over the period for each model. Emissions are summed to obtain the total emission flux over the considered region. Mixing ratio, wind speed and planetary boundary layer height are averaged for grid points over the ocean, with non-zero emissions and less than 90% sea ice cover. The open ocean fraction is computed as one minus the average of the sea ice concentration over the considered region. Panels (i,j) only include the 9 models providing the *bldep* variables (i.e. all except BCC-ESM, CNRM-ESM and MRI-ESM). Panels (c,d) do not include BCC-ESM as emission rates are not available for that model. CNRM-ESM is not included in this analysis.

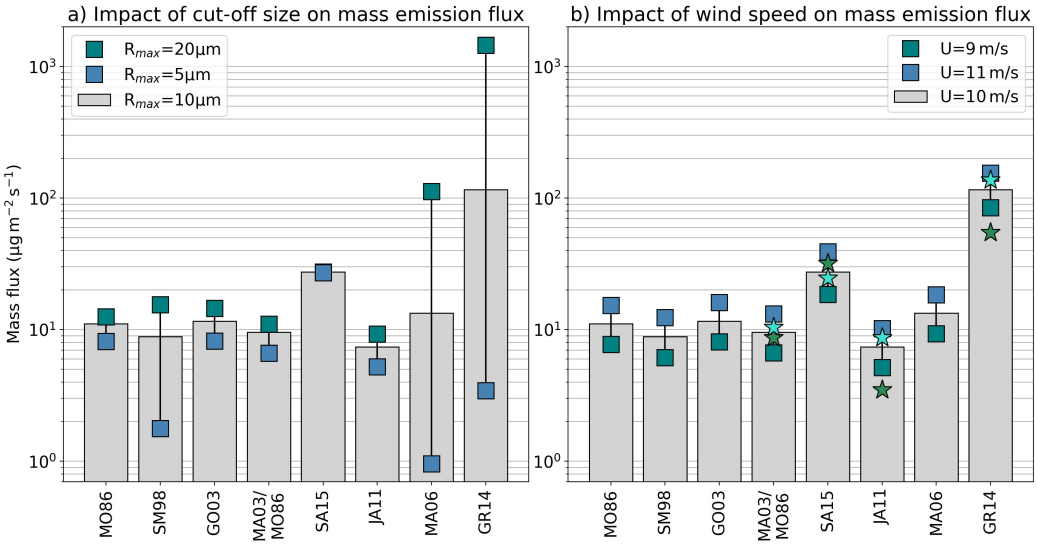

Figure 6. Sea salt aerosol source functions used in CMIP6 models. a) effect on the mass emission flux of changing the aerosol cut-off radius, at 10 m s^{-1} wind speed and 5°C SST. b) effect of changing wind speed on the mass emission flux for a cut-off radius at 10 µm. Green and blue stars indicate mass emission fluxes for 0 and 10°C SST, respectively, at 10 m s^{-1} wind speed. In both panels, size bin limits are taken as 0.05-0.5-1-R_{max} µm.

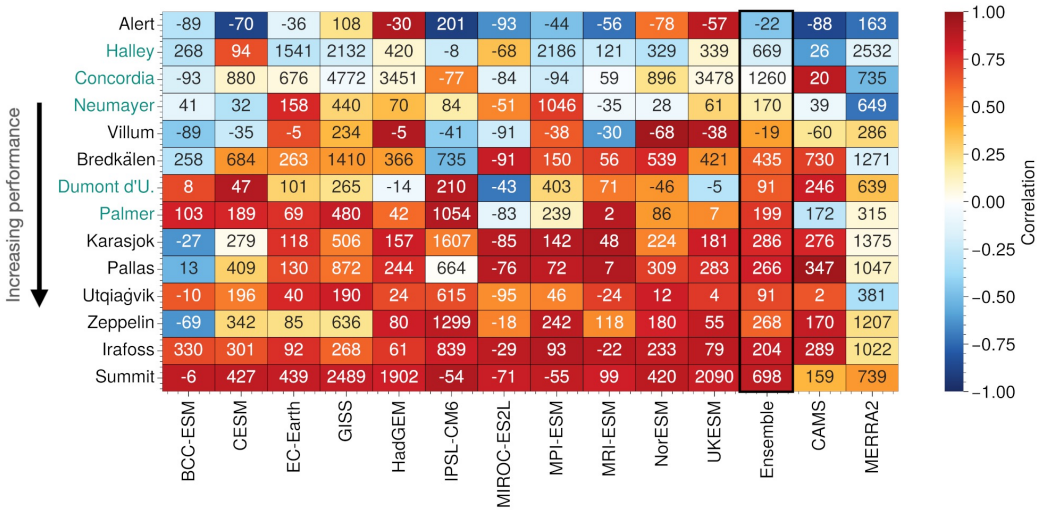

Figure 7. Normalized mean bias (numbers, in percent) and Pearson correlation coefficient (colormap) with respect to 9 stations in the Arctic (in black) and 5 stations in the Antarctic (in blue). CMIP6 individual models and ensemble mean are for the period 1951–2014, CAMS reanalysis is for 2003–2021 and MERRA2 is for 1980–2021. See Figures 8 and A2 for individual comparisons of time series.

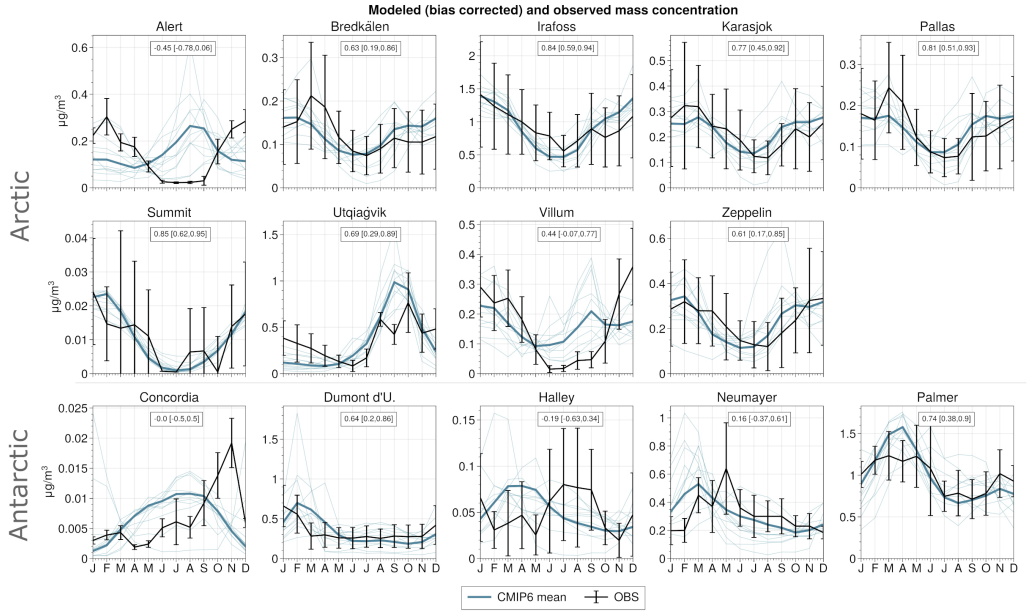

Figure 8. Annual cycle of sodium aerosol surface mass concentrations at 9 stations in the Arctic (top and middle) and 5 stations in the Antarctic (bottom). Observations are in black (caps show one standard deviation of monthly means), individual CMIP6 models (1951–2014) are in light blue, CMIP6 ensemble mean (solid thick line) is in blue. CMIP6 values are bias corrected by applying a factor ¡OBS¿/¡MODEL¿. Boxes indicate the Pearson correlation coefficient between the annual cycle in CMIP6 ensemble mean and observations, with the 95% confidence interval between brackets.

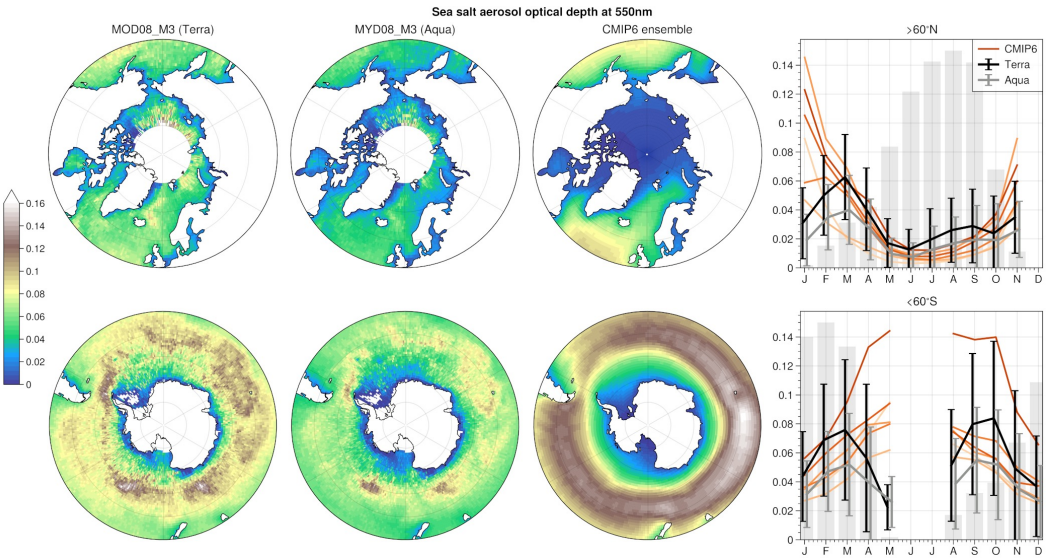

Figure 9. CMIP6 ensemble median and MODIS Terra (MOD08_M3) and Aqua (MYD08_M3) Dark Target/Deep Blue sea salt aerosol optical depth at 550 nm. Both MODIS data sets and CMIP6 model data are averages of monthly means for the period 2005–2014. The CMIP6 ensemble contains a subset of models providing the *od550ss* variable (BCC-ESM, EC-Earth, IPSL-CM6, MPI-ESM, MRI-ESM, NorESM). MODIS values are adjusted to only account for the contribution to AOD of particles with Angstrom exponent below 1. Right: average annual cycles of sea salt aerosol optical depth in MODIS (Terra in black, Aqua in grey - caps show one standard deviation) and CMIP6 models (orange). MODIS and CMIP6 values are colocated, i.e. CMIP6 values are used only for those grid cells where MODIS has valid records. Gray bars indicate, on an arbitrary scale common to both panels, the number of available records in MODIS Terra.

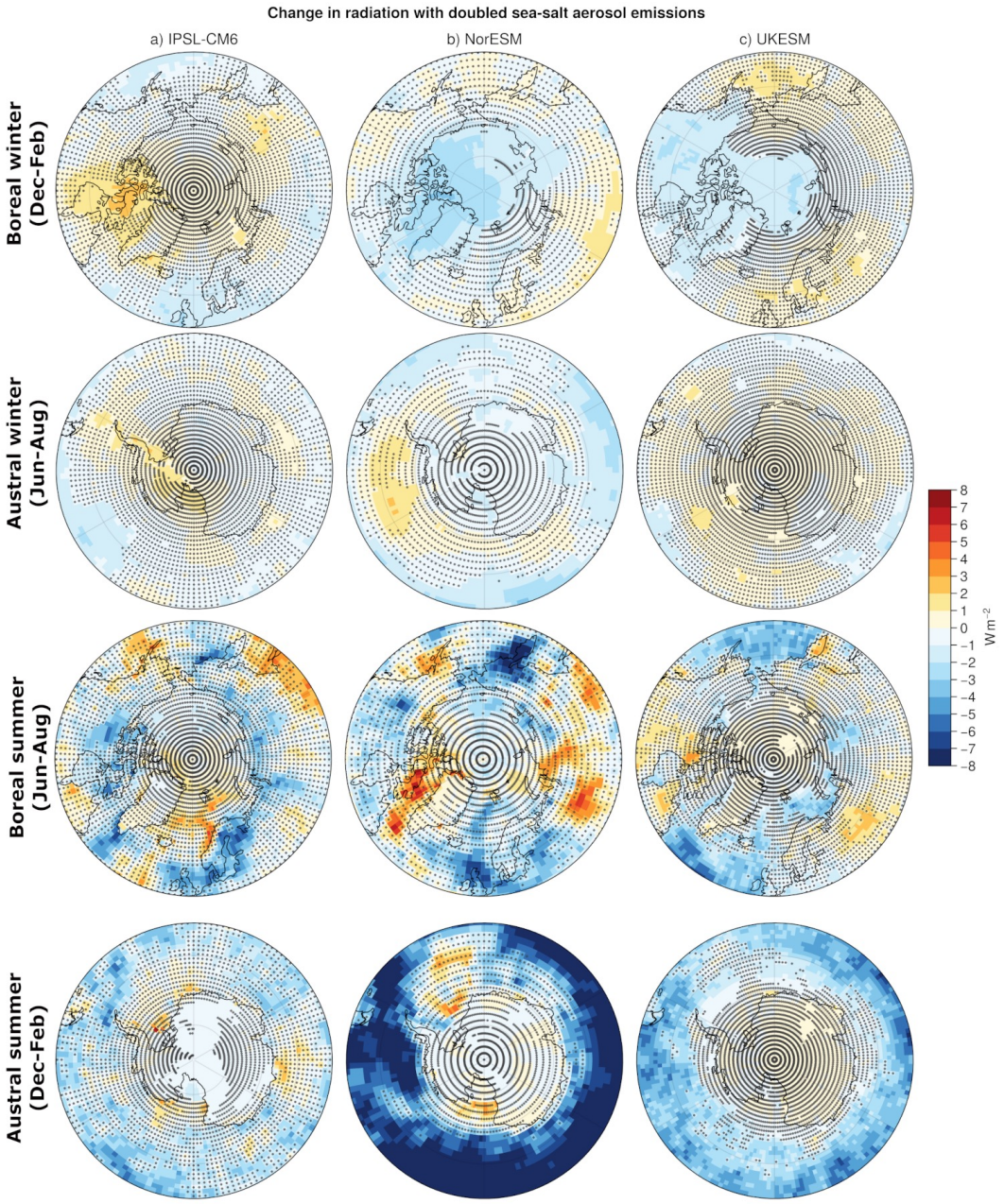

Figure 10. Change in top-of-the-atmosphere net downward radiative flux (*rtmt*) in a scenario with doubled sea salt aerosol emissions under pre-industrial atmospheric composition (30 years under 1850 conditions). Stippling shows the grid points for which the difference between *piClim-2xss* and *piClim-control* is not significant at the 90% level according to a Wilcoxon test.

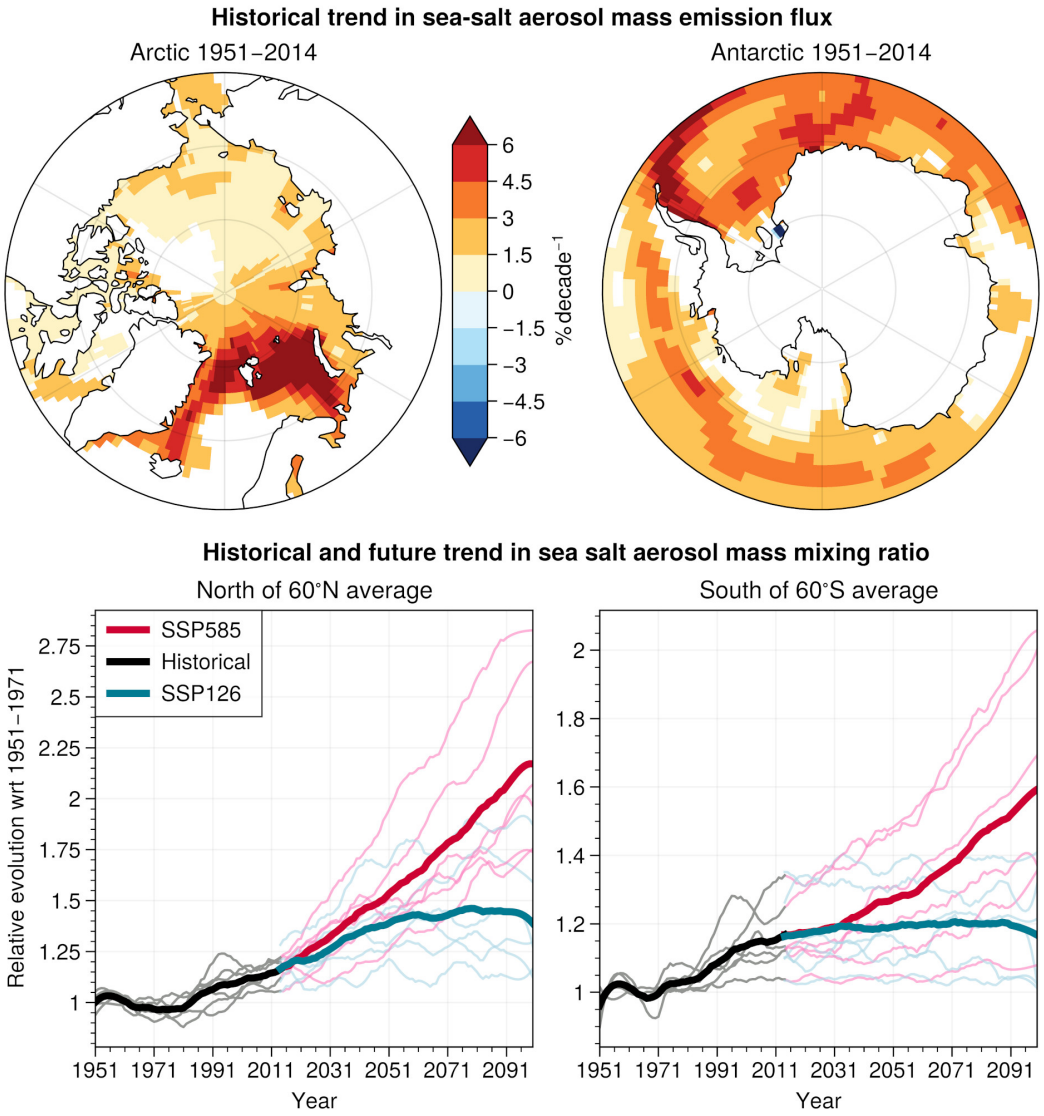

Figure 11. Top: trends in sea salt aerosol mass emissions in the ensemble mean for the period 1951–2014. The mass emission is normalized by the 1951–2014 average to obtain %/decade. Bottom: historical and future (relative to the 1951–1971 mean) yearly time series (1951–2099) of average sea salt surface mass mixing ratio north of 60°N (left) and south of 60°S (right), including ocean and land. Mixing ratios are weighted by grid cell area for spatial averaging. Time series are smoothed using a Savitzky-Golay filter with a window length of 19 years and a polynomial order 3. Ensemble means are shown as thicker lines (black for the historical period, blue for SSP126, red for SSP585). Individual members use the same color code but with thinner lines. Included models are: GISS, HadGEM, MIROC-ES2L, MRI-ESM, NorESM and UKESM. The smallest (largest, respectively) trend in SSP585 corresponds to NorESM (UKESM, respectively).

Appendix A

Table A1. Regionally averaged mean change in surface temperature (*tas* variable - °C) in the CMIP6 ensemble of models GISS, HadGEM, MIROC-ES2L, MRI-ESM, NorESM and UKESM. This change is computed as the difference between the 2000–2014 historical and 2085–2100 future averages. Arctic is all grid points north of 60°N, Antarctic is all grid points south of 60°S. Spread here refers to the difference between the model with largest increase and the model with smallest increase.

	Global		**Arctic**		**Antarctic**	
	Mean	Spread	Mean	Spread	Mean	Spread
SSP126	1.5	2.0	3.8	7.4	1.0	1.5
SSP585	5.1	3.8	10.8	10.0	4.5	3.1

A1 Sea salt dominance assessed from MACv2

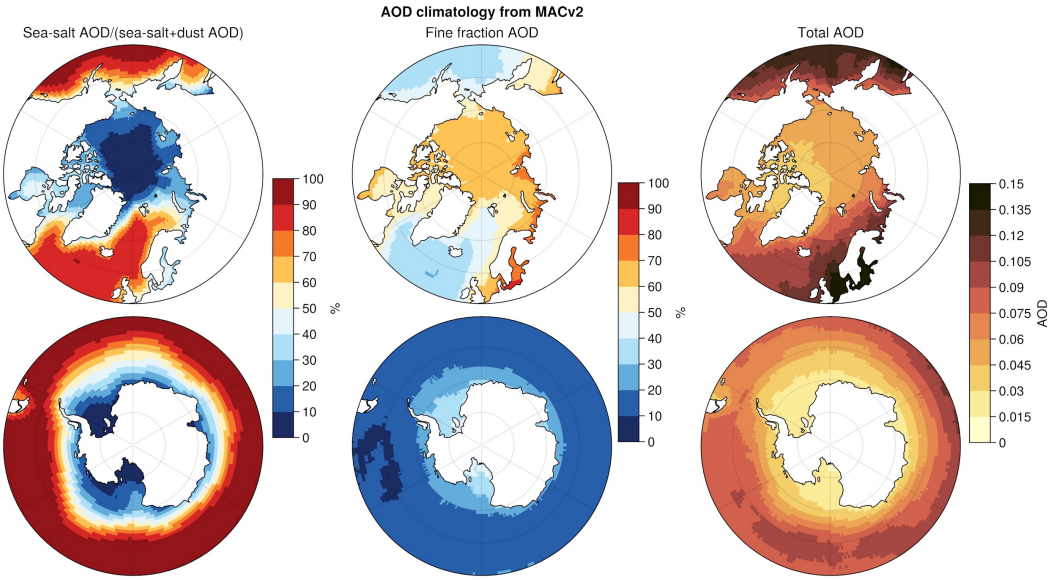

Figure A1. AOD characteristics at the poles from the MACv2 climatology (Kinne, 2019). Left: fraction of coarse AOD (dust+sea salt) attributed to sea salt (annual average climatology). Only dust and sea salt are considered here since we look at the coarse fraction AOD. Middle: fraction of total AOD from fine mode aerosols. Right: total AOD.

A2 Non-normalized annual cycles versus observations

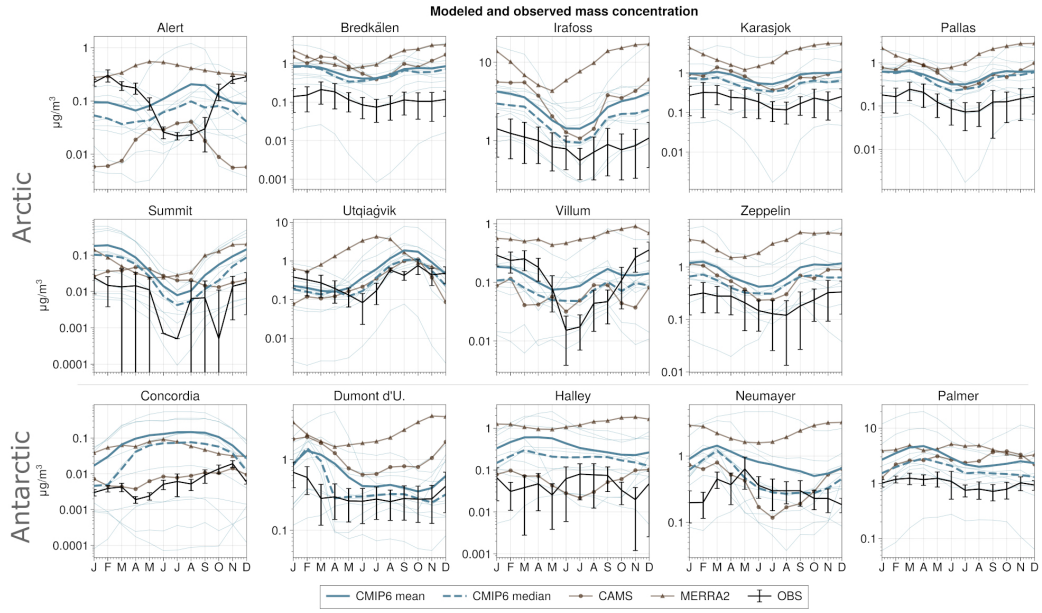

Figure A2. Annual cycle of sodium aerosol surface mass concentrations at 9 stations in the Arctic (top and middle) and 5 stations in the Antarctic (bottom). Observations are in black (caps show one standard deviation of monthly means), individual CMIP6 models (1951–2014) are in light blue, CMIP6 ensemble mean (solid line) and median (dashed line) is in darker blue, reanalyses (CAMS 2003–2021 - circles - and MERRA2 1980–2021 - triangles) are in brown.

957 ## A3 Annual cycles at Alert

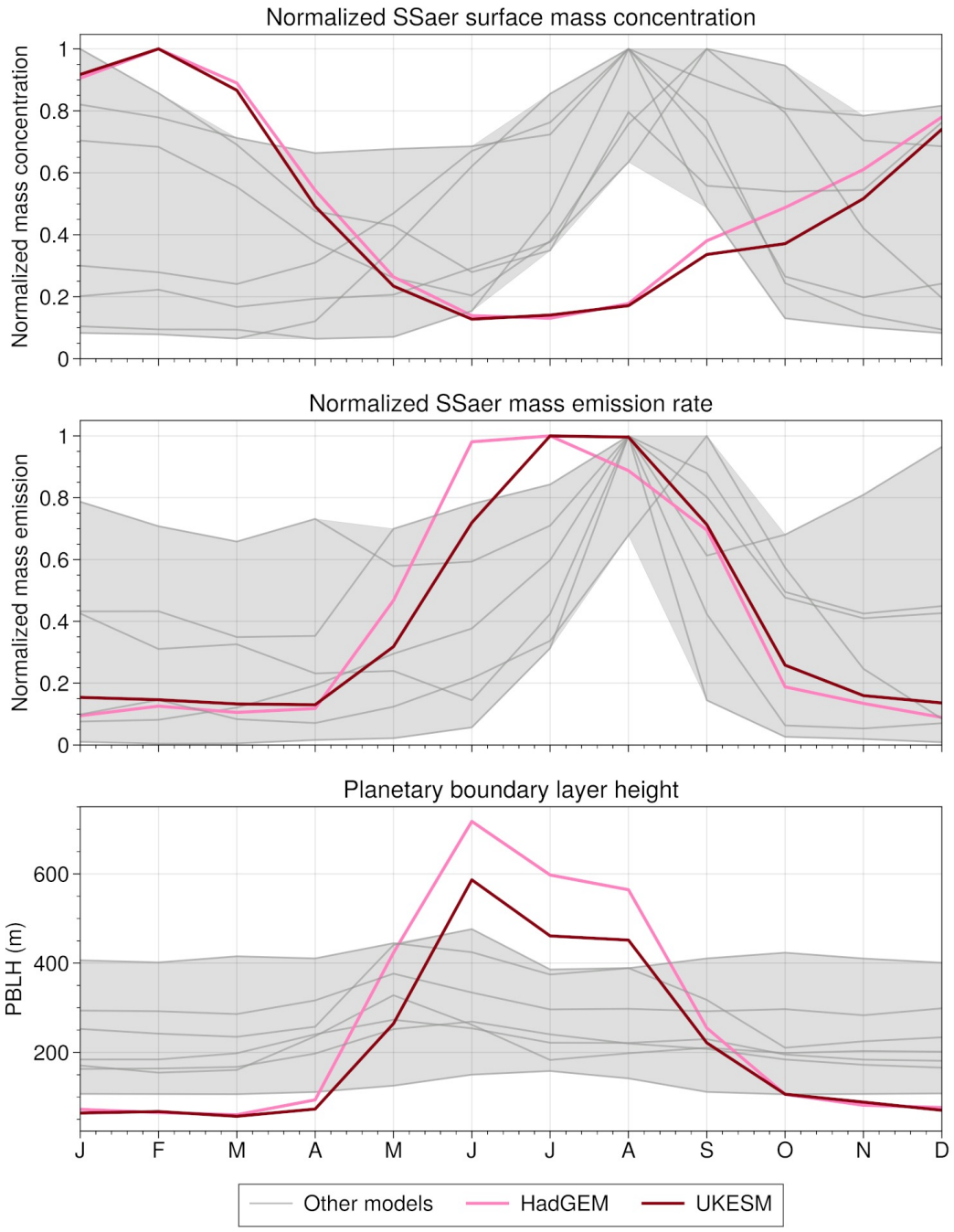

Figure A3. Annual cycles of SSaer mass concentration (top - normalized), SSaer mass emission (middle - normalized) and boundary layer height (bottom) in CMIP6 at the grid point nearest to the Alert station. Average annual cycles for the period 1951–2014.

A4 Vertical distribution of SSaer and clouds

The evaluation conducted in Section 3.1 mainly focused on surface and column-integrated SSaer variables. To connect SSaer to clouds, information on the vertical distribution is needed. Figure A4 shows the regionally averaged profiles of *mmrss* in the Arctic and Antarctic in the historical period, in Jun–Aug and Dec–Feb. This figure shows that the diversity at the surface affects also the vertical distribution. The inter-model spread is roughly constant from the surface up to 400 m altitude and remains above 1 $\mu g\, g^{-1}$ at 10 km altitude in winter months. Given that SSaer are injected high enough to interact with clouds (Figure A4), part of the diversity in cloud profiles at the poles could stem from this diversity in SSaer profile. In summer months, the profiles converge more rapidly.

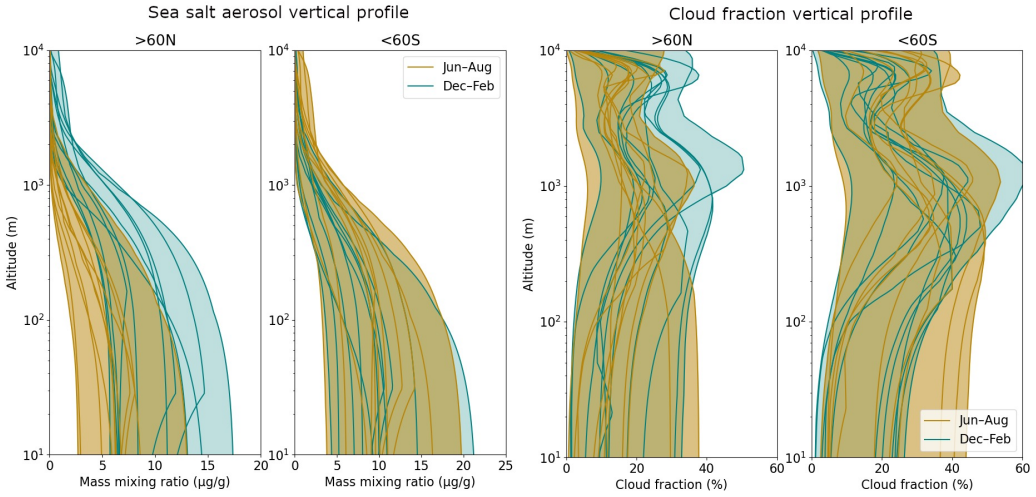

Figure A4. Left: Average vertical profile of sea salt aerosol mass mixing ratio in the Arctic (above 60°N - left) and Antarctic (below 60°S - right) in individual CMIP6 models, for Jun–Aug (blue) and Dec–Feb (yellow). Each line corresponds to one model, and the shaded area marks the ensemble envelope. Only grid points with less than 50% sea ice concentration are considered in this figure. Right: same as left but for cloud fraction. NB: the vertical axis is in logarithmic scale.

968 ## A5 *piClim*-2x*ss* scenario

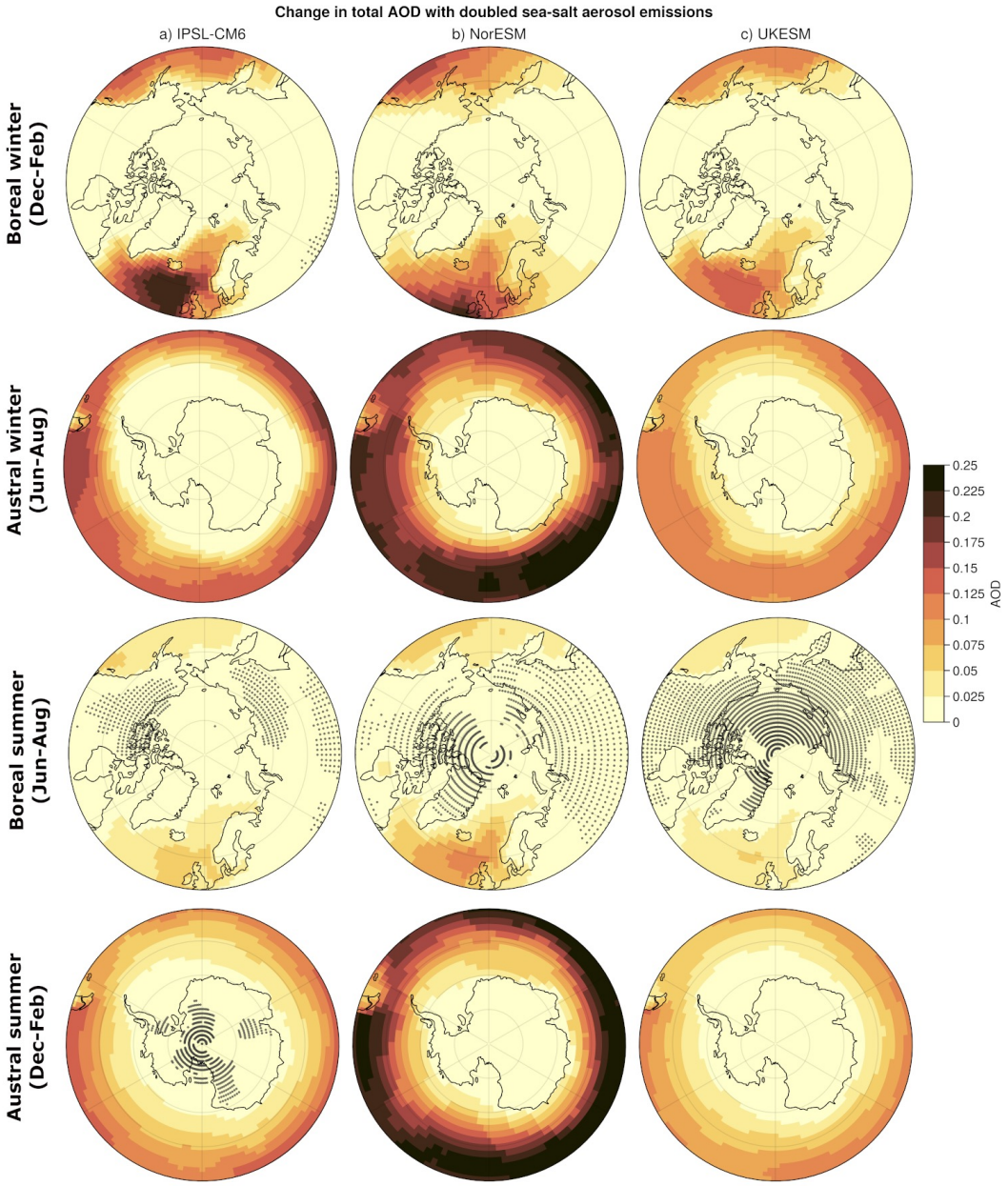

Figure A5. Same as Figure 10 but for total aerosol optical depth ($od550aer$).

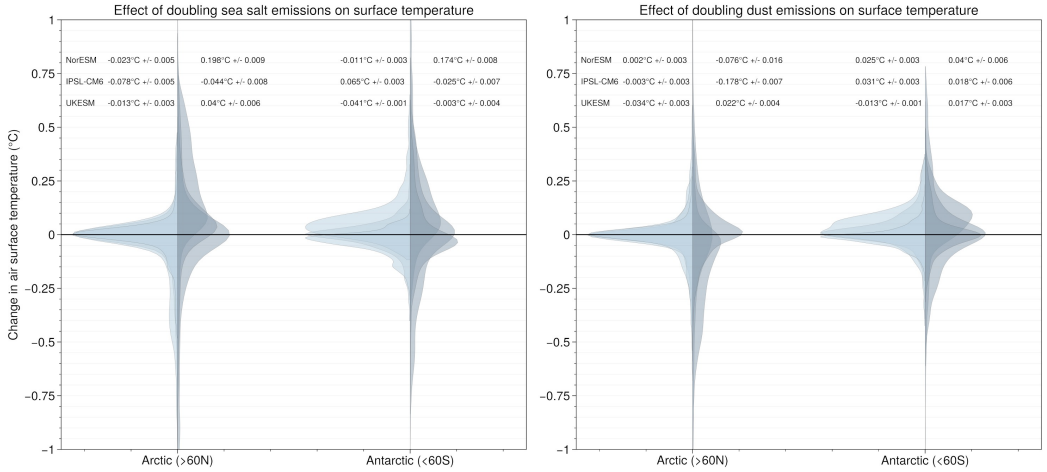

Figure A6. Difference in air surface temperature in the *piClim-control* and the *piClim-*2x*ss* (left) and *piClim-*2x*dust* (right) experiments. Models included: IPSL-CM6, NorESM and UKESM. Summer is Jun–Aug in the Arctic, Dec–Feb in the Antarctic, and vice-versa. Values along the x-axis indicate the normalized frequency of temperature changes.

969 ## A6 Drivers of sea salt emission trends

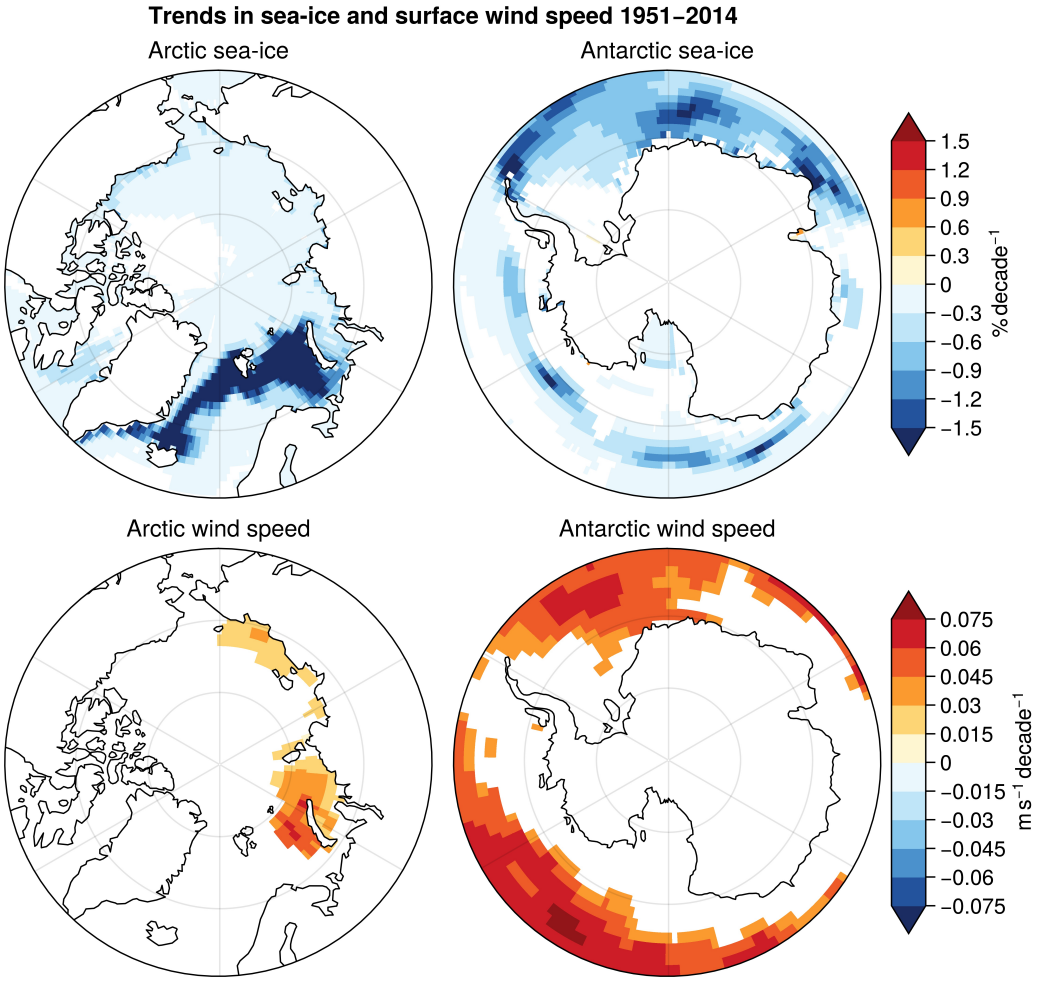

Figure A7. Historical trends in sea ice concentration (top) and surface wind speed (bottom) in CMIP6 models for the period 1951–2014. Included models are: GISS, HadGEM, MIROC-ES2L, MRI-ESM, NorESM and UKESM. Trends are computed following Mann-Kendall's test. Only significant trends at the 95% level are shown.

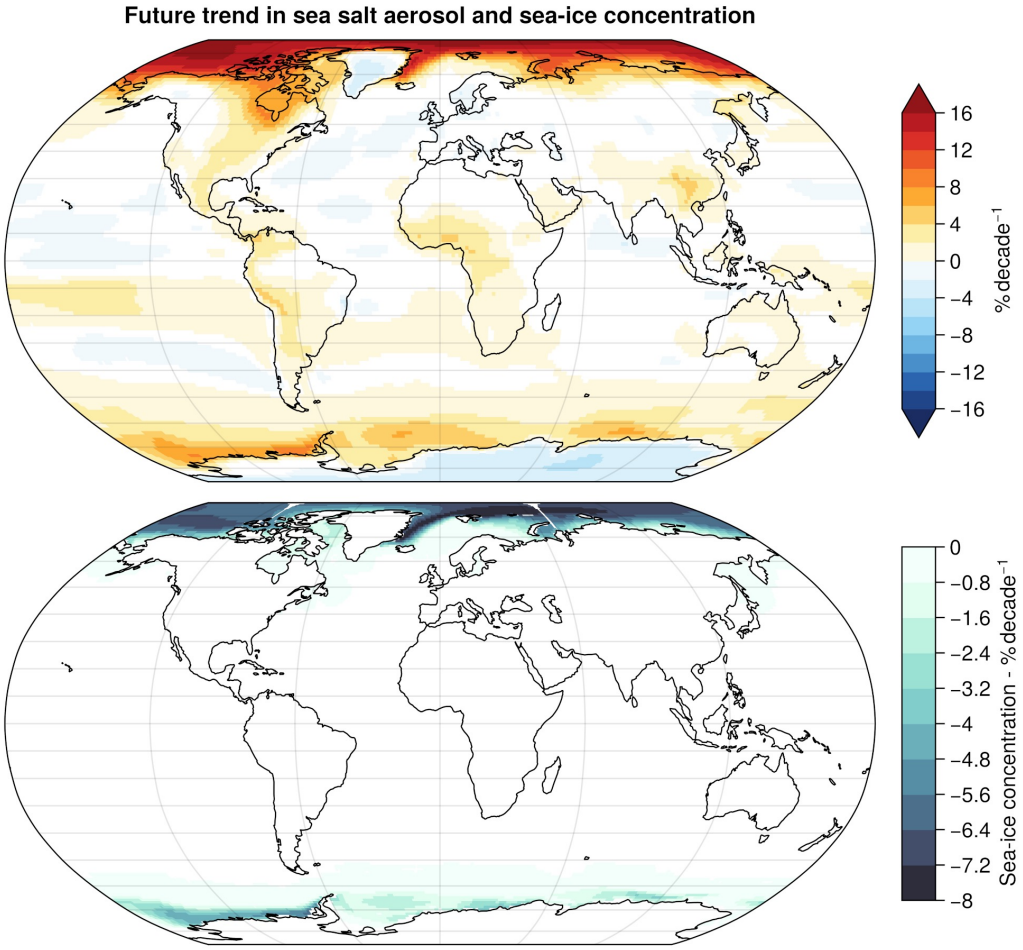

Figure A8. Maps of future trends in annual mean sea salt aerosol surface mass mixing ratio (top) and sea-ice concentration (bottom). Scenario SSP585. Multi-model mean from GISS, HadGEM, MIROC-ES2L, MRI-ESM, NorESM and UKESM.

Open Research

The scripts used for computations and figure creation can be found at the following repository: `https://github.com/rlapere/CMIP6_SSA_Paper`

Author contributions

RL: Conceptualization, Methodology, Formal analysis, Investigation, Writing - Original Draft, Visualization. JT: Conceptualization, Methodology, Supervision, Writing - Original Draft. LM: Conceptualization, Methodology, Supervision, Writing - Review & Editing. MF, ML, BS, LS, XY, AE, RM, AR, MES, MS, PZ: Methodology, Writing - Review & Editing.

Acknowledgments
This project has received funding from the European Union's Horizon 2020 research and innovation programme under grant agreement No 101003826 via project CRiceS (Climate Relevant interactions and feedbacks: the key role of sea ice and Snow in the polar and global climate system). The authors also acknowledge the EU H2020 FORCeS project, contract No 821205. We also appreciate the effort of the CMIP6 modelling groups which contributed the data to the CMIP6 data archive. We acknowledge Yves Balkanski, Jean-Christophe Raut and Dirk Olivié for the fruitful discussions.

References

Alkama, R., Taylor, P. C., Garcia-San Martin, L., Douville, H., Duveiller, G., Forzieri, G., ... Cescatti, A. (2020). Clouds damp the radiative impacts of polar sea ice loss. *The Cryosphere*, *14*, 2673–2686. doi: 10.5194/tc-14-2673-2020

Allen, R. J., & Sherwood, S. C. (2011). The impact of natural versus anthropogenic aerosols on atmospheric circulation in the Community Atmosphere Model. *Climate Dynamics*, *36*, 1959–1978. doi: 10.1007/s00382-010-0898-8

Andreae, M. O., & Rosenfeld, D. (2008). Aerosol–cloud–precipitation interactions. Part 1. The nature and sources of cloud-active aerosols. *Earth-Science Reviews*, *89*, 13–41. doi: 10.1016/j.earscirev.2008.03.001

Atmoko, D., & Lin, T.-H. (2022). Sea Salt Aerosol Identification Based on Multispectral Optical Properties and Its Impact on Radiative Forcing over the Ocean. *Remote Sensing*, *14*, 3188. doi: 10.3390/rs14133188

Bian, H., Froyd, K., Murphy, D. M., Dibb, J., Darmenov, A., Chin, M., ... Smirnov, A. (2019). Observationally constrained analysis of sea salt aerosol in the marine atmosphere. *Atmospheric Chemistry and Physics*, *19*, 10773–10785. doi: 10.5194/acp-19-10773-2019

Boucher, O., Randall, D., Artaxo, P., Bretherton, C., Feingold, G., Forster, P., ... Zhang, X. Y. (2013). Climate Change 2013: The Physical Science Basis. Contribution of Working Group I to the Fifth Assessment Report of the Intergovernmental Panel on Climate Change [Stocker, T.F., D. Qin, G.-K. Plattner, M. Tignor, S.K. Allen, J. Boschung, A. Nauels, Y. Xia, V. Bex and P.M. Midgley (eds.)]. In (pp. 571–657). Cambridge University Press, Cambridge, UK and New York, NY, USA. doi: 10.1017/CBO9781107415324.016

Boucher, O., Servonnat, J., Albright, A. L., Aumont, O., Balkanski, Y., Bastrikov, V., ... Vuichard, N. (2020). Presentation and Evaluation of the IPSL-CM6A-LR Climate Model. *Journal of Advances in Modeling Earth Systems*, *12*, e2019MS002010. doi: 10.1029/2019MS002010

Browse, J., Carslaw, K. S., Mann, G. W., Birch, C. E., Arnold, S. R., & Leck, C. (2014). The complex response of Arctic aerosol to sea-ice retreat. *Atmospheric Chemistry and Physics*, *14*, 7543–7557. doi: 10.5194/acp-14-7543-2014

Burgos, M. A., Andrews, E., Titos, G., Benedetti, A., Bian, H., Buchard, V., ... Zieger, P. (2020). A global model–measurement evaluation of particle light scattering coefficients at elevated relative humidity. *Atmospheric Chemistry and Physics*, *20*, 10231–10258. doi: 10.5194/acp-20-10231-2020

Cai, Z., You, Q., Wu, F., Chen, H. W., Chen, D., & Cohen, J. (2021). Arctic Warming Revealed by Multiple CMIP6 Models: Evaluation of Historical Simulations and Quantification of Future Projection Uncertainties. *Journal of Climate*, *34*, 4871–4892. doi: 10.1175/JCLI-D-20-0791.1

Chen, Y., Cheng, Y., Ma, N., Wei, C., Ran, L., Wolke, R., ... Wiedensohler, A. (2020). Natural sea-salt emissions moderate the climate forcing of anthropogenic nitrate. *Atmospheric Chemistry and Physics*, *20*, 771–786. doi: 10.5194/acp-20-771-2020

Curry, J. A., Schramm, J. L., Rossow, W. B., & Randall, D. (1996). Overview of Arctic Cloud and Radiation Characteristics. *Journal of Climate*, *9*, 1731–1764. doi: 10.1175/1520-0442(1996)009⟨1731:OOACAR⟩2.0.CO;2

Dada, L., Angot, H., Beck, I., Baccarini, A., Quéléver, L. L. J., Boyer, M., ... Schmale, J. (2022). A central arctic extreme aerosol event triggered by a warm air-mass intrusion. *Nature Communications*, *13*, 1–15. doi: 10.1038/s41467-022-32872-2

Danabasoglu, G., Lamarque, J.-F., Bacmeister, J., Bailey, D. A., DuVivier, A. K., Edwards, J., ... Strand, W. G. (2020). The Community Earth System Model Version 2 (CESM2). *Journal of Advances in Modeling Earth Systems*, *12*, e2019MS001916. doi: 10.1029/2019MS001916

Dasarathy, S., Kar, J., Tackett, J., Rodier, S. D., Lu, X., Vaughan, M., ... Bowman, J. S. (2021). Multi-Year Seasonal Trends in Sea Ice, Chlorophyll Concentration, and Marine Aerosol Optical Depth in the Bellingshausen Sea. *Journal of Geophysical Research: Atmospheres*, *126*, e2021JD034737. doi: 10.1029/2021JD034737

DeMott, P. J., Hill, T. C. J., McCluskey, C. S., Prather, K. A., Collins, D. B., Sullivan, R. C., ... Franc, G. D. (2016). Sea spray aerosol as a unique source of ice nucleating particles. *Proc Natl Acad Sci U S A*, *113*, 5797–5803. doi: 10.1073/pnas.1514034112

Diaconescu, E. P., Mailhot, A., Brown, R., & Chaumont, D. (2018). Evaluation of CORDEX-Arctic daily precipitation and temperature-based climate indices over Canadian Arctic land areas. *Clim Dyn*, *50*, 2061–2085. doi: 10.1007/s00382-017-3736-4

Dror, T., Lehahn, Y., Altaratz, O., & Koren, I. (2018). Temporal-Scale Analysis of Environmental Controls on Sea Spray Aerosol Production Over the South Pacific Gyre. *Geophysical Research Letters*, *45*, 8637–8646. doi: 10.1029/2018GL078707

Döscher, R., Acosta, M., Alessandri, A., Anthoni, P., Arsouze, T., Bergman, T., ... Zhang, Q. (2022). The EC-Earth3 Earth system model for the Coupled Model Intercomparison Project 6. *Geoscientific Model Development*, *15*, 2973–3020. doi: 10.5194/gmd-15-2973-2022

Eastman, R., & Warren, S. G. (2010). Interannual Variations of Arctic Cloud Types in Relation to Sea Ice. *Journal of Climate*, *23*, 4216–4232. doi: 10.1175/2010JCLI3492.1

ESGF. (2014). The Earth System Grid Federation: An open infrastructure for access to distributed geospatial data. *Future Gener. Comput. Syst*, *36*, 400–417. doi: 10.1016/j.future.2013.07.002

Fanourgakis, G. S., Kanakidou, M., Nenes, A., Bauer, S. E., Bergman, T., Carslaw, K. S., ... Yu, F. (2019). Evaluation of global simulations of aerosol particle and cloud condensation nuclei number, with implications for cloud droplet formation. *Atmospheric Chemistry and Physics*, *19*, 8591–8617. doi: 10.5194/acp-19-8591-2019

Flato, G., Marotzke, J., Abiodun, B., Braconnot, P., Chou, S. C., Collins, W., ... Rummukainen, M. (2013). Climate change 2013: The physical science basis. contribution of working group i to the fifth assessment report of the intergovernmental panel on climate change [stocker, t.f., d. qin, g.-k. plattner, m. tignor, s.k. allen, j. boschung, a. nauels, y. xia, v. bex and p.m. midgley (eds.)]. In (pp. 741–882). Cambridge University Press, Cambridge, UK and New York, NY, USA. doi: 10.1017/CBO9781107415324.020

Fossum, K. N., Ovadnevaite, J., Ceburnis, D., Dall'Osto, M., Marullo, S., Bellacicco, M., ... O'Dowd, C. (2018). Summertime Primary and Secondary Contributions to Southern Ocean Cloud Condensation Nuclei. *Sci Rep*, *8*, 13844. doi: 10.1038/s41598-018-32047-4

Fossum, K. N., Ovadnevaite, J., Ceburnis, D., Preißler, J., Snider, J. R., Huang, R.-J., ... O'Dowd, C. (2020). Sea-spray regulates sulfate cloud droplet activation over oceans. *npj Climate and Atmospheric Science*, *3*, 1–6. doi: 10.1038/s41612-020-0116-2

Frey, M. M., Norris, S. J., Brooks, I. M., Anderson, P. S., Nishimura, K., Yang, X., ... Wolff, E. W. (2020). First direct observation of sea salt aerosol production from blowing snow above sea ice. *Atmospheric Chemistry and Physics*, *20*, 2549–2578. doi: 10.5194/acp-20-2549-2020

Gliß, J., Mortier, A., Schulz, M., Andrews, E., Balkanski, Y., Bauer, S. E., ... Tsyro, S. G. (2021). AeroCom phase III multi-model evaluation of the aerosol life cycle and optical properties using ground- and space-based remote sensing as well as surface in situ observations. *Atmospheric Chemistry and Physics*, *21*, 87–128. doi: 10.5194/acp-21-87-2021

Gong, S. L. (2003). A parameterization of sea-salt aerosol source function for sub- and super-micron particles. *Global Biogeochemical Cycles*, *17*. doi: 10.1029/2003GB002079

Gryspeerdt, E., Goren, T., Sourdeval, O., Quaas, J., Mülmenstädt, J., Dipu, S., ... Christensen, M. (2019). Constraining the aerosol influence on cloud liquid water path. *Atmospheric Chemistry and Physics*, *19*, 5331–5347. doi: 10.5194/acp-19-5331-2019

Grythe, H., Ström, J., Krejci, R., Quinn, P., & Stohl, A. (2014). A review of sea-spray aerosol source functions using a large global set of sea salt aerosol concentration measurements. *Atmospheric Chemistry and Physics*, *14*, 1277–1297. doi: 10.5194/acp-14-1277-2014

Gutjahr, O., Putrasahan, D., Lohmann, K., Jungclaus, J. H., von Storch, J.-S., Brueggemann, N., ... Stössel, A. (2019). Max Planck Institute Earth System Model (MPI-ESM1.2) for the High-Resolution Model Intercomparison Project (HighResMIP). *Geoscientific Model Development*, *12*, 3241–3281. doi: 10.5194/gmd-12-3241-2019

Hajima, T., Watanabe, M., Yamamoto, A., Tatebe, H., Noguchi, M. A., Abe, M., ... Kawamiya, M. (2020). Development of the MIROC-ES2L Earth system model and the evaluation of biogeochemical processes and feedbacks. *Geoscientific Model Development*, *13*, 2197–2244. doi: 10.5194/gmd-13-2197-2020

Hall, A. (2004). The Role of Surface Albedo Feedback in Climate. *Journal of Climate*, *17*, 1550–1568. doi: 10.1175/1520-0442(2004)017⟨1550:TROSAF⟩2.0.CO;2

Hara, K., Osada, K., Yabuki, M., Takashima, H., Theys, N., & Yamanouchi, T. (2018). Important contributions of sea-salt aerosols to atmospheric bromine cycle in the Antarctic coasts. *Sci Rep*, *8*, 13852. doi: 10.1038/s41598-018-32287-4

Held, A., Brooks, I. M., Leck, C., & Tjernström, M. (2011). On the potential contribution of open lead particle emissions to the central Arctic aerosol concentration. *Atmospheric Chemistry and Physics*, *11*, 3093–3105. doi: 10.5194/acp-11-3093-2011

Heslin-Rees, D., Burgos, M., Hansson, H.-C., Krejci, R., Ström, J., Tunved, P., & Zieger, P. (2020). From a polar to a marine environment: has the changing Arctic led to a shift in aerosol light scattering properties? *Atmospheric Chemistry and Physics*, *20*, 13671–13686. doi: 10.5194/acp-20-13671-2020

Holtslag, A. a. M., Svensson, G., Baas, P., Basu, S., Beare, B., Beljaars, A. C. M., ... Wiel, B. J. H. V. D. (2013). Stable Atmospheric Boundary Layers and Diurnal Cycles: Challenges for Weather and Climate Models. *Bulletin of the American Meteorological Society*, *94*, 1691–1706. doi: 10.1175/BAMS-D-11-00187.1

Huang, J., & Jaeglé, L. (2017). Wintertime enhancements of sea salt aerosol in polar regions consistent with a sea ice source from blowing snow. *Atmospheric Chemistry and Physics*, *17*, 3699–3712. doi: 10.5194/acp-17-3699-2017

Huang, Y., Ding, Q., Dong, X., Xi, B., & Baxter, I. (2021). Summertime low clouds mediate the impact of the large-scale circulation on Arctic sea ice. *Commun Earth Environ*, *2*, 1–10. doi: 10.1038/s43247-021-00114-w

Ioannidis, E., Law, K. S., Raut, J.-C., Marelle, L., Onishi, T., Kirpes, R. M., ... Pratt, K. A. (2022). *Modelling wintertime Arctic Haze and sea-spray aerosols* (Tech. Rep.). Aerosols/Atmospheric Modelling/Troposphere/Chemistry (chemical composition and reactions). doi: 10.5194/egusphere-2022-310

Jaeglé, L., Quinn, P. K., Bates, T. S., Alexander, B., & Lin, J.-T. (2011). Global distribution of sea salt aerosols: new constraints from in situ and remote sensing observations. *Atmospheric Chemistry and Physics*, *11*, 3137–3157. doi: 10.5194/acp-11-3137-2011

Kinne, S. (2019). The MACv2 aerosol climatology. *Tellus B: Chemical and Physical Meteorology*, *71*, 1–21. doi: 10.1080/16000889.2019.1623639

Kirpes, R. M., Bonanno, D., May, N. W., Fraund, M., Barget, A. J., Moffet, R. C., ... Pratt, K. A. (2019). Wintertime Arctic Sea Spray Aerosol Composition Controlled by Sea Ice Lead Microbiology. *ACS Cent. Sci.*, *5*, 1760–1767. doi: 10.1021/acscentsci.9b00541

Korhonen, H., Carslaw, K. S., Forster, P. M., Mikkonen, S., Gordon, N. D., & Kokkola, H. (2010). Aerosol climate feedback due to decadal increases in Southern Hemisphere wind speeds. *Geophysical Research Letters*, *37*. doi: 10.1029/2009GL041320

Kramer, S. J., Alvarez, C., Barkley, A. E., Colarco, P. R., Custals, L., Delgadillo, R., ... Zuidema, P. (2020). Apparent dust size discrepancy in aerosol reanalysis in north African dust after long-range transport. *Atmospheric Chemistry and Physics*, *20*, 10047–10062. doi: 10.5194/acp-20-10047-2020

Lachlan-Cope, T. (2010). Antarctic clouds. *Polar Research*, *29*, 150–158. doi: 10.3402/polar.v29i2.6065

Legrand, M., Yang, X., Preunkert, S., & Theys, N. (2016). Year-round records of sea salt, gaseous, and particulate inorganic bromine in the atmospheric boundary layer at coastal (Dumont d'Urville) and central (Concordia) East Antarctic sites. *Journal of Geophysical Research: Atmospheres*, *121*, 997–1023. doi: 10.1002/2015JD024066

Levine, J. G., Yang, X., Jones, A. E., & Wolff, E. W. (2014). Sea salt as an ice core proxy for past sea ice extent: A process-based model study. *Journal of Geophysical Research: Atmospheres*, *119*, 5737–5756. doi: 10.1002/2013JD020925

Li, S.-M., & Barrie, L. A. (1993). Biogenic sulfur aerosol in the Arctic troposphere: 1. Contributions to total sulfate. *Journal of Geophysical Research: Atmospheres*, *98*, 20613–20622. doi: 10.1029/93JD02234

Liu, S., Liu, C.-C., Froyd, K. D., Schill, G. P., Murphy, D. M., Bui, T. P., ... Gao, R.-S. (2021). Sea spray aerosol concentration modulated by sea surface temperature. *Proceedings of the National Academy of Sciences*, *118*, e2020583118. doi: 10.1073/pnas.2020583118

Mahowald, N. M., Lamarque, J.-F., Tie, X. X., & Wolff, E. (2006). Sea-salt aerosol

response to climate change: Last Glacial Maximum, preindustrial, and doubled carbon dioxide climates. *Journal of Geophysical Research: Atmospheres*, *111*. doi: 10.1029/2005JD006459

Manabe, S., & Wetherald, R. T. (1975). The Effects of Doubling the CO2 Concentration on the climate of a General Circulation Model. *Journal of the Atmospheric Sciences*, *32*, 3–15. doi: 10.1175/1520-0469(1975)032⟨0003:TEODTC⟩2.0.CO;2

Mann, H. (1945). Nonparametric tests against trend. *Econometrica: Journal of the Econometric Society*, 245-259. doi: 10.2307/1907187

Marelle, L., Thomas, J. L., Ahmed, S., Tuite, K., Stutz, J., Dommergue, A., ... Baladima, F. (2021). Implementation and Impacts of Surface and Blowing Snow Sources of Arctic Bromine Activation Within WRF-Chem 4.1.1. *Journal of Advances in Modeling Earth Systems*, *13*, e2020MS002391. doi: 10.1029/2020MS002391

McCrystall, M. R., Stroeve, J., Serreze, M., Forbes, B. C., & Screen, J. A. (2021). New climate models reveal faster and larger increases in Arctic precipitation than previously projected. *Nature Communications*, *12*, 6765. doi: 10.1038/s41467-021-27031-y

Mei, L., Xue, Y., de Leeuw, G., von Hoyningen-Huene, W., Kokhanovsky, A. A., Istomina, L., ... Burrows, J. P. (2013). Aerosol optical depth retrieval in the Arctic region using MODIS data over snow. *Remote Sensing of Environment*, *128*, 234–245. doi: 10.1016/j.rse.2012.10.009

Meinander, O., Dagsson-Waldhauserova, P., Amosov, P., Aseyeva, E., Atkins, C., Baklanov, A., ... Vukovic Vimic, A. (2022). Newly identified climatically and environmentally significant high-latitude dust sources. *Atmospheric Chemistry and Physics*, *22*, 11889–11930. doi: 10.5194/acp-22-11889-2022

Meredith, M., Sommerkorn, M., Cassotta, S., Derksen, C., Ekaykin, A., Hollowed, A., ... Schuur, E. (2019). IPCC Special Report on the Ocean and Cryosphere in a Changing Climate [H.-O. Pörtner, D. C. Roberts, V. Masson-Delmotte, P. Zhai, M. Tignor, E. Poloczanska, K. Mintenbeck, A. Alegría, M. Nicolai, A. Okem, J. Petzold, B. Rama, N. M. Weyer (eds.)]. In (p. 203-320). Cambridge University Press, Cambridge, UK and New York, NY, USA. doi: 10.1017/9781009157964.005

Miller, R. L., Schmidt, G. A., Nazarenko, L. S., Bauer, S. E., Kelley, M., Ruedy, R., ... Yao, M.-S. (2021). CMIP6 Historical Simulations (1850–2014) With GISS-E2.1. *Journal of Advances in Modeling Earth Systems*, *13*, e2019MS002034. doi: 10.1029/2019MS002034

Monahan, E. C., Spiel, D. E., & Davidson, K. L. (1986). A Model of Marine Aerosol Generation Via Whitecaps and Wave Disruption. In E. C. Monahan & G. M. Niocaill (Eds.), *Oceanic Whitecaps: And Their Role in Air-Sea Exchange Processes* (pp. 167–174). Springer Netherlands. doi: 10.1007/978-94-009-4668-2_16

Mortier, A., Gliß, J., Schulz, M., Aas, W., Andrews, E., Bian, H., ... Tilmes, S. (2020). Evaluation of climate model aerosol trends with ground-based observations over the last 2 decades – an AeroCom and CMIP6 analysis. *Atmospheric Chemistry and Physics*, *20*, 13355–13378. doi: 10.5194/acp-20-13355-2020

Murphy, D. M., Froyd, K. D., Bian, H., Brock, C. A., Dibb, J. E., DiGangi, J. P., ... Yu, P. (2019). The distribution of sea-salt aerosol in the global troposphere. *Atmospheric Chemistry and Physics*, *19*, 4093–4104. doi: 10.5194/acp-19-4093-2019

Myhre, G., Shindell, D., Bréon, F.-M., Collins, W., Fuglestvedt, J., Huang, J., ... Zhang, H. (2013). Climate Change 2013: The Physical Science Basis. Contribution of Working Group I to the Fifth Assessment Report of the Intergovernmental Panel on Climate Change [Stocker, T.F., D. Qin, G.-K. Plattner, M. Tignor, S.K. Allen, J. Boschung, A. Nauels, Y. Xia, V. Bex and P.M. Midgley

(eds.)]. In (chap. Anthropogenic and Natural Radiative Forcing). Cambridge University Press, Cambridge, UK and New York, NY, USA.

Mårtensson, E. M., Nilsson, E. D., de Leeuw, G., Cohen, L. H., & Hansson, H.-C. (2003). Laboratory simulations and parameterization of the primary marine aerosol production. *Journal of Geophysical Research: Atmospheres*, *108*. doi: 10.1029/2002JD002263

Nilsson, E. D., Rannik, U., Swietlicki, E., Leck, C., Aalto, P. P., Zhou, J., & Norman, M. (2001). Turbulent aerosol fluxes over the Arctic Ocean: 2. Wind-driven sources from the sea. *Journal of Geophysical Research: Atmospheres*, *106*, 32139–32154. doi: 10.1029/2000JD900747

Norwegian Institute for Air Research. (2022). *Ebas.* Retrieved from `https://ebas.nilu.no/`

Notz, D., & SIMIP Community. (2020). Arctic Sea Ice in CMIP6. *Geophysical Research Letters*, *47*, e2019GL086749. doi: 10.1029/2019GL086749

O'Neill, B. C., Tebaldi, C., van Vuuren, D. P., Eyring, V., Friedlingstein, P., Hurtt, G., ... Sanderson, B. M. (2016). The Scenario Model Intercomparison Project (ScenarioMIP) for CMIP6. *Geoscientific Model Development*, *9*, 3461–3482. doi: 10.5194/gmd-9-3461-2016

Palerme, C., Genthon, C., Claud, C., Kay, J. E., Wood, N. B., & L'Ecuyer, T. (2017). Evaluation of current and projected Antarctic precipitation in CMIP5 models. *Climate Dynamics*, *48*, 225–239. doi: 10.1007/s00382-016-3071-1

Platnick, S. (2015). *MODIS Atmosphere L3 Monthly Product.* (NASA MODIS Adaptive Processing System, Goddard Space Flight Center, USA. Access date: 20 July 2022, doi: 10.5067/MODIS/MOD08_M3.006) doi: 10.5067/MODIS/MOD08_M3.006

Prank, M., Tonttila, J., Ahola, J., Kokkola, H., Kühn, T., Romakkaniemi, S., & Raatikainen, T. (2022). Impacts of marine organic emissions on low-level stratiform clouds – a large eddy simulator study. *Atmospheric Chemistry and Physics*, *22*, 10971–10992. doi: 10.5194/acp-22-10971-2022

Qi, L., Li, Q., Li, Y., & He, C. (2017). Factors controlling black carbon distribution in the Arctic. *Atmospheric Chemistry and Physics*, *17*, 1037–1059. doi: 10.5194/acp-17-1037-2017

Quinn, P. K., Coffman, D. J., Johnson, J. E., Upchurch, L. M., & Bates, T. S. (2017). Small fraction of marine cloud condensation nuclei made up of sea spray aerosol. *Nature Geosci*, *10*, 674–679. doi: 10.1038/ngeo3003

Quinn, P. K., Miller, T. L., Bates, T. S., Ogren, J. A., Andrews, E., & Shaw, G. E. (2002). A 3-year record of simultaneously measured aerosol chemical and optical properties at Barrow, Alaska. *Journal of Geophysical Research: Atmospheres*, *107*, 8–15. doi: 10.1029/2001JD001248

Rantanen, M., Karpechko, A. Y., Lipponen, A., Nordling, K., Hyvärinen, O., Ruosteenoja, K., ... Laaksonen, A. (2022). The Arctic has warmed nearly four times faster than the globe since 1979. *Commun Earth Environ*, *3*, 1–10. doi: 10.1038/s43247-022-00498-3

Regayre, L. A., Schmale, J., Johnson, J. S., Tatzelt, C., Baccarini, A., Henning, S., ... Carslaw, K. S. (2020). The value of remote marine aerosol measurements for constraining radiative forcing uncertainty. *Atmospheric Chemistry and Physics*, *20*, 10063–10072. doi: 10.5194/acp-20-10063-2020

Rhodes, R. H., Yang, X., & Wolff, E. W. (2018). Sea Ice Versus Storms: What Controls Sea Salt in Arctic Ice Cores? *Geophysical Research Letters*, *45*, 5572–5580. doi: 10.1029/2018GL077403

Roach, L. A., Dörr, J., Holmes, C. R., Massonnet, F., Blockley, E. W., Notz, D., ... Bitz, C. M. (2020). Antarctic Sea Ice Area in CMIP6. *Geophysical Research Letters*, *47*, e2019GL086729. doi: 10.1029/2019GL086729

Roussel, M.-L., Lemonnier, F., Genthon, C., & Krinner, G. (2020). Brief communication: Evaluating Antarctic precipitation in ERA5 and CMIP6

against CloudSat observations. *The Cryosphere*, *14*, 2715–2727. doi: 10.5194/tc-14-2715-2020

Salter, M. E., Zieger, P., Acosta Navarro, J. C., Grythe, H., Kirkevåg, A., Rosati, B., ... Nilsson, E. D. (2015). An empirically derived inorganic sea spray source function incorporating sea surface temperature. *Atmospheric Chemistry and Physics*, *15*, 11047–11066. doi: 10.5194/acp-15-11047-2015

Samset, B. H. (2022). Aerosol absorption has an underappreciated role in historical precipitation change. *Communications Earth & Environment*, *3*, 1–8. doi: 10.1038/s43247-022-00576-6

Sand, M., Samset, B. H., Balkanski, Y., Bauer, S., Bellouin, N., Berntsen, T. K., ... Zhang, H. (2017). Aerosols at the poles: an AeroCom Phase II multi-model evaluation. *Atmospheric Chemistry and Physics*, *17*, 12197–12218. doi: 10.5194/acp-17-12197-2017

Sand, M., Samset, B. H., Myhre, G., Gliß, J., Bauer, S. E., Bian, H., ... Watson-Parris, D. (2021). Aerosol absorption in global models from AeroCom phase III. *Atmospheric Chemistry and Physics*, *21*, 15929–15947. doi: 10.5194/acp-21-15929-2021

Satheesh, S. K., & Lubin, D. (2003). Short wave versus long wave radiative forcing by Indian Ocean aerosols: Role of sea-surface winds. *Geophysical Research Letters*, *30*. doi: 10.1029/2003GL017499

Schmale, J., Zieger, P., & Ekman, A. M. L. (2021). Aerosols in current and future Arctic climate. *Nat. Clim. Chang.*, *11*, 95–105. doi: 10.1038/s41558-020-00969-5

Schulzweida, U., Kornblueh, L., & Quast, R. (2012). *Climate Data Operators User's Guide - Version 1.5.9* (Tech. Rep.). MPI for Meteorology, Brockmann Consult.

Seinfeld, J. H., & Pandis, S. N. (2016). *Atmospheric Chemistry and Physics: From Air Pollution to Climate Change, 3rd Edition*. Wiley.

Seland, O., Bentsen, M., Olivié, D., Toniazzo, T., Gjermundsen, A., Graff, L. S., ... Schulz, M. (2020). Overview of the Norwegian Earth System Model (NorESM2) and key climate response of CMIP6 DECK, historical, and scenario simulations. *Geoscientific Model Development*, *13*, 6165–6200. doi: 10.5194/gmd-13-6165-2020

Sellar, A. A., Walton, J., Jones, C. G., Wood, R., Abraham, N. L., Andrejczuk, M., ... Griffiths, P. T. (2020). Implementation of U.K. Earth System Models for CMIP6. *Journal of Advances in Modeling Earth Systems*, *12*, e2019MS001946. doi: 10.1029/2019MS001946

Smith, D. M., Screen, J. A., Deser, C., Cohen, J., Fyfe, J. C., García-Serrano, J., ... Zhang, X. (2019). The Polar Amplification Model Intercomparison Project (PAMIP) contribution to CMIP6: investigating the causes and consequences of polar amplification. *Geoscientific Model Development*, *12*, 1139–1164. doi: 10.5194/gmd-12-1139-2019

Smith, M. H., & Harrison, N. M. (1998). The sea spray generation function. *Journal of Aerosol Science*, *29*, S189–S190. doi: 10.1016/S0021-8502(98)00280-8

Sogacheva, L., Popp, T., Sayer, A. M., Dubovik, O., Garay, M. J., Heckel, A., ... Arola, A. (2020). Merging regional and global aerosol optical depth records from major available satellite products. *Atmospheric Chemistry and Physics*, *20*, 2031–2056. doi: 10.5194/acp-20-2031-2020

Struthers, H., Ekman, A. M. L., Glantz, P., Iversen, T., Kirkevag, A., Seland, O., ... Nilsson, E. D. (2013). Climate-induced changes in sea salt aerosol number emissions: 1870 to 2100. *Journal of Geophysical Research: Atmospheres*, *118*, 670–682. doi: 10.1002/jgrd.50129

Struthers, H., Ekman, A. M. L., Glantz, P., Iversen, T., Kirkevåg, A., Mårtensson, E. M., ... Nilsson, E. D. (2011). The effect of sea ice loss on sea salt aerosol concentrations and the radiative balance in the Arctic. *Atmospheric Chemistry*

and Physics, *11*, 3459–3477. doi: 10.5194/acp-11-3459-2011

Stuecker, M. F., Bitz, C. M., Armour, K. C., Proistosescu, C., Kang, S. M., Xie, S.-P., ... Jin, F.-F. (2018). Polar amplification dominated by local forcing and feedbacks. *Nature Climate Change*, *8*, 1076–1081. doi: 10.1038/s41558-018-0339-y

Séférian, R., Nabat, P., Michou, M., Saint-Martin, D., Voldoire, A., Colin, J., ... Madec, G. (2019). Evaluation of CNRM Earth System Model, CNRM-ESM2-1: Role of Earth System Processes in Present-Day and Future Climate. *J. Adv. Model. Earth Syst.*, *11*, 4182–4227. doi: 10.1029/2019MS001791

Takemura, T., Nakajima, T., Dubovik, O., Holben, B. N., & Kinne, S. (2002). Single-Scattering Albedo and Radiative Forcing of Various Aerosol Species with a Global Three-Dimensional Model. *Journal of Climate*, *15*, 333–352. doi: 10.1175/1520-0442(2002)015⟨0333:SSAARF⟩2.0.CO;2

Tang, M. S. Y., Chenoli, S. N., Samah, A. A., & Hai, O. S. (2018). An assessment of historical Antarctic precipitation and temperature trend using CMIP5 models and reanalysis datasets. *Polar Science*, *15*, 1–12. doi: 10.1016/j.polar.2018.01.001

Tewari, K., Mishra, S. K., Salunke, P., & Dewan, A. (2022). Future projections of temperature and precipitation for Antarctica. *Environmental Research Letters*, *17*, 014029. doi: 10.1088/1748-9326/ac43e2

Thornhill, G., Collins, W., Olivié, D., Skeie, R. B., Archibald, A., Bauer, S., ... Weber, J. (2021). Climate-driven chemistry and aerosol feedbacks in CMIP6 Earth system models. *Atmospheric Chemistry and Physics*, *21*, 1105–1126. doi: 10.5194/acp-21-1105-2021

Tunved, P., Ström, J., & Krejci, R. (2013). Arctic aerosol life cycle: linking aerosol size distributions observed between 2000 and 2010 with air mass transport and precipitation at Zeppelin station, Ny-Ålesund, Svalbard. *Atmospheric Chemistry and Physics*, *13*, 3643–3660. doi: 10.5194/acp-13-3643-2013

Turner, J., Comiso, J. C., Marshall, G. J., Lachlan-Cope, T. A., Bracegirdle, T., Maksym, T., ... Orr, A. (2009). Non-annular atmospheric circulation change induced by stratospheric ozone depletion and its role in the recent increase of Antarctic sea ice extent. *Geophysical Research Letters*, *36*. doi: 10.1029/2009GL037524

Vavrus, S. J., & Alkama, R. (2022). Future trends of arctic surface wind speeds and their relationship with sea ice in CMIP5 climate model simulations. *Clim Dyn*, *59*, 1833–1848. doi: 10.1007/s00382-021-06071-6

Wilson, T. W., Ladino, L. A., Alpert, P. A., Breckels, M. N., Brooks, I. M., Browse, J., ... Murray, B. J. (2015). A marine biogenic source of atmospheric ice-nucleating particles. *Nature*, *525*, 234–238. doi: 10.1038/nature14986

Wu, T., Zhang, F., Zhang, J., Jie, W., Zhang, Y., Wu, F., ... Hu, A. (2020). Beijing Climate Center Earth System Model version 1 (BCC-ESM1): model description and evaluation of aerosol simulations. *Geoscientific Model Development*, *13*, 977–1005. doi: 10.5194/gmd-13-977-2020

Xian, P., Zhang, J., O'Neill, N. T., Toth, T. D., Sorenson, B., Colarco, P. R., ... Ranjbar, K. (2022). Arctic spring and summertime aerosol optical depth baseline from long-term observations and model reanalyses – Part 1: Climatology and trend. *Atmospheric Chemistry and Physics*, *22*, 9915–9947. doi: 10.5194/acp-22-9915-2022

Xu, W., Ovadnevaite, J., Fossum, K. N., Lin, C., Huang, R.-J., Ceburnis, D., & O'Dowd, C. (2022). Sea spray as an obscured source for marine cloud nuclei. *Nat. Geosci.*, *15*, 282–286. doi: 10.1038/s41561-022-00917-2

Yang, X., Frey, M. M., Rhodes, R. H., Norris, S. J., Brooks, I. M., Anderson, P. S., ... Wolff, E. W. (2019). Sea salt aerosol production via sublimating wind-blown saline snow particles over sea ice: parameterizations and relevant microphysical mechanisms. *Atmospheric Chemistry and Physics*, *19*, 8407–8424. doi:

10.5194/acp-19-8407-2019

Yang, X., Pyle, J. A., & Cox, R. A. (2008). Sea salt aerosol production and bromine release: Role of snow on sea ice. *Geophysical Research Letters*, *35*. doi: 10.1029/2008GL034536

Yukimoto, S., Kawai, H., Koshiro, T., Oshima, N., Yoshida, K., Urakawa, S., ... Ishii, M. (2019). The Meteorological Research Institute Earth System Model Version 2.0, MRI-ESM2.0: Description and Basic Evaluation of the Physical Component. *Journal of the Meteorological Society of Japan*, *97*, 931–965. doi: 10.2151/jmsj.2019-051

Zhu, L., Jacob, D. J., Eastham, S. D., Sulprizio, M. P., Wang, X., Sherwen, T., ... Percival, C. J. (2019). Effect of sea salt aerosol on tropospheric bromine chemistry. *Atmospheric Chemistry and Physics*, *19*, 6497–6507. doi: 10.5194/acp-19-6497-2019

Zieger, P., Väisänen, O., Corbin, J. C., Partridge, D. G., Bastelberger, S., Mousavi-Fard, M., ... Salter, M. E. (2017). Revising the hygroscopicity of inorganic sea salt particles. *Nature Communications*, *8*, 15883. doi: 10.1038/ncomms15883

Zinke, J., Nilsson, E. D., Zieger, P., & Salter, M. E. (2022). The Effect of Seawater Salinity and Seawater Temperature on Sea Salt Aerosol Production. *Journal of Geophysical Research: Atmospheres*, *127*, e2021JD036005. doi: 10.1029/2021JD036005

Zábori, J., Krejci, R., Ekman, A. M. L., Mårtensson, E. M., Ström, J., de Leeuw, G., & Nilsson, E. D. (2012). Wintertime Arctic Ocean sea water properties and primary marine aerosol concentrations. *Atmospheric Chemistry and Physics*, *12*, 10405–10421. doi: 10.5194/acp-12-10405-2012